

## ABSTRACT

Title of dissertation: SUPERCONDUCTORS THAT BREAK  
TIME-REVERSAL SYMMETRY

Lance L. Boyer  
Doctor of Philosophy, 2019

Dissertation directed by: Professor Victor M. Yakovenko  
Department of Physics

Since 2006 it has been discovered experimentally that the superconducting state spontaneously breaks time-reversal symmetry (TRS) in several materials, such as  $\text{Sr}_2\text{RuO}_4$ ,  $\text{UPt}_3$ ,  $\text{URu}_2\text{Si}_2$ ,  $\text{PrOs}_4\text{Sb}_{12}$ , and Bi/Ni bilayers. This dissertation studies three physical phenomena related to time-reversal symmetry breaking (TRSB) in these superconductors.

The experimental evidence for TRSB comes from the magneto-optical polar Kerr effect, which is determined by the high frequency ac Hall conductivity. However, these superconductors are also expected to exhibit a spontaneous dc Hall effect in the absence of an applied magnetic field. In the first part of this dissertation we propose a method for measuring the low frequency Hall conductivity in superconductors with TRSB. The method is based on a Corbino disk geometry where an oscillating co-axial magnetic field induces circular electric field, which, in turn, induces radial charge oscillations due to the Hall conductivity.

In the second part, we propose an explanation for the polar Kerr effect observed in the Hidden-Order phase of the heavy-fermion superconductor  $\text{URu}_2\text{Si}_2$ . Using a

Ginzburg-Landau model for a complex order parameter, we show that the system can have a metastable ferromagnetic state, which produces the Kerr signal, even if the Hidden-Order state respects TRS. We predict that applying a reversed magnetic field should reset the system to the non-magnetic ground state, resulting in zero Kerr signal.

In the third part of the dissertation, we investigate the conditions for the existence of a Majorana bound state on a vortex in a 2D  $d_{xy} + id_{x^2-y^2}$  superconductor with strong spin-orbit coupling. This TRSB pairing was proposed earlier for the Ni/Bi bilayer. We find that the Majorana bound state can exist for a  $d_{xy} + id_{x^2-y^2}$  pairing under conditions similar to those for s-wave pairing.

SUPERCONDUCTORS THAT BREAK  
TIME-REVERSAL SYMMETRY

by

Lance L. Boyer

Dissertation submitted to the Faculty of the Graduate School of the  
University of Maryland, College Park in partial fulfillment  
of the requirements for the degree of  
Doctor of Philosophy  
2019

Advisory Committee:  
Professor Victor M. Yakovenko, Chair/Advisor  
Professor Steven Anlage  
Assistant Professor Maissam Barkeshli  
Professor Theodore Einstein  
Associate Professor Jeremy Munday

© Copyright by  
Lance L. Boyer  
2019



# Table of Contents

Table of Contents	ii
List of Figures	iv
List of Abbreviations	vi
1 Background	1
1.1 Phenomenological Superconductivity	1
1.2 Time-Reversal Symmetry Breaking	7
1.3 Magneto-Optical Polar Kerr Effect	9
2 The Hall Effect as a Probe of Time-Reversal Symmetry Breaking in Superconductors	14
2.1 Introduction	14
2.2 Electrodynamics of Superconductors	16
2.3 AC Meissner Screening for $\sigma_H = 0$	18
2.4 Radial Charge Oscillation for $\sigma_H \neq 0$	23
2.5 Estimating the Hall Conductivity	26
2.6 Experimental Proposal	29
2.7 Induced Hall Conductivity	32
2.8 Charge Oscillation in General	34
2.8.1 Local Oscillation in Charge Density	34
2.8.2 Oscillation in Total Surface Charge	37
2.9 Solenoid Threading the Superconductor	39
2.9.1 Field in “Vacuum” $R_s < r < R_i$	41
2.9.2 Screening in the Superconductor $r > R_i$	42
2.9.3 Radial Charge Oscillation	48
2.10 Conclusions	52
3 URu <sub>2</sub> Si <sub>2</sub> and Metastable Magnetism in the HO Phase	55
3.1 Introduction	55
3.2 URu <sub>2</sub> Si <sub>2</sub>	57
3.3 Haule-Kotliar Model	60
3.4 Competition of Hidden Order and Antiferromagnetism	64
3.5 Competition of Hidden Order and Ferromagnetism	65
3.6 Field-Reversal Test	68

3.7	Comparison with Experiment . . . . .	70
3.8	The magnetic field terminating hidden order . . . . .	72
3.9	The Staggered Magnetic Moment . . . . .	74
3.10	Conclusions . . . . .	75
4	Majorana Modes in Bi/Ni Bilayers . . . . .	77
4.1	Introduction . . . . .	77
4.2	Majorana Quasiparticles . . . . .	79
4.3	The BdG Hamiltonian . . . . .	81
4.4	Spin-Orbit-Pseudospin . . . . .	82
4.5	Radial BdG Equation . . . . .	85
4.6	Solving the BdG Equation in the Electron Sector . . . . .	86
4.7	Inside the Vortex Core ( $\Delta' = 0$ ) . . . . .	88
4.8	Outside the Vortex Core ( $\Delta' \neq 0$ ) . . . . .	89
4.9	Matching solutions at $r = \xi$ . . . . .	91
4.10	Conclusions . . . . .	93
	Bibliography . . . . .	95

## List of Figures

1.1	Schematic diagram of a simplified Sagnac interferometer in which a beam and its reciprocal under time-reversal interact with a sample and then interfere at the detector. Since the beam paths are reciprocal with respect to time-reversal, only a time-reversal symmetry breaking sample produces a signal. (Credit: This figure was modified from a freely available Creative Commons image owned by Wikipedia user Krishnavedala.) . . . . .	10
2.1	Our setup consists of a superconducting cylinder of inner radius $R_i$ , outer radius $R_o$ and length $L$ . Most effects occur near the outer edge of the superconductor. . . . .	19
2.2	Our proposed experimental setup uses a waveguide nozzle at the end of a coaxial cable to measure the potential difference $V_r^H$ . The thick black lines represent insulating coating on the inside of the waveguide, so that the voltage measurement is contactless. The applied magnetic field $\mathbf{B}_0$ of the external solenoid is represented by purple arrows. . . . .	30
2.3	A solenoid of radius $R_s$ threading an superconducting annular cylinder of inner radius $R_i$ , outer radius $R_o$ , and length $L$ . The axial magnetic field $\mathbf{B}_s$ of the solenoid induces radial Hall current $j_r^H$ which is compensated by radial supercurrent $j_r^S$ within a London penetration depth $\lambda_L$ of the inner surface of the superconductor. Since the effects happen near the inner surface of the superconductor, the outer radius $R_o$ can be taken to be infinite. . . . .	40



3.1	This figure shows the $A_{2g}$ symmetry breaking of the local $5f^2$ electron wavefunctions. (A) The crystal structure and wavefunctions are presented in the paramagnetic state. The high-temperature wavefunctions have two vertical mirror plane symmetries $\sigma_v$ and $\sigma_d$ . (B) A schematic band structure of the low-lying states and conduction band is shown. (C) The crystal structure remains the same below the transition temperature, but the hybridized wavefunctions break the vertical mirror plane symmetries and pick up chirality. (D) An antiferromagnetic ordering of chiralities is shown, indicating a chirality density wave. Figure from Ref. 1. Reprinted with permission from AAAS.	61
3.2	Phase diagram for the free energy in Eq. (3.5) as a function of magnetic energy $b$ and temperature $T$ . The numbers in circles and the degree of shading indicate the number of minima of $f[\psi_{\text{HO}}, \psi_{\text{FM}}]$ . Every shaded domain has two degenerate HO minima with $ \psi_{\text{HO}}  \neq 0$ and may have one or two FM minima with $\psi_{\text{FM}} > 0$ or $\psi_{\text{FM}} < 0$ , as schematically indicated around $T = 10$ K. The HO (FM) minima have lower energy to the left (right) of the dashed first-order transition line labeled I. The solid line labeled II represents a second-order phase transition from paramagnetism to HO. Blue, red, and green lines represent the Zero-Field Cooling (ZFC), High-Field Cooling (HFC), and Field-Reversal Test (FRT) protocols.	66
3.3	Contour plots of the free energy $f[\psi_{\text{HO}}, \psi_{\text{AF}}]$ given by Eq. (3.4) or $f[\psi_{\text{HO}}, \psi_{\text{FM}}]$ given by Eq. (3.5) for points A-H in Fig. 3.2. The horizontal and vertical axes represent the non-magnetic, $\psi_{\text{HO}}$ , and magnetic, $\psi_{\text{AF}}$ for (a)-(c) and $\psi_{\text{FM}}$ for (a)-(i), components of the order parameter. Global minima, local minima, and saddle points are indicated by red disks, orange squares, and black triangles, while red arrows indicate the state of the system reached following the paths in Fig. 3.2.	69
3.4	Phase diagram as in Fig. 3.2 recalculated using $\Delta = 7$ K and $\gamma = 525$ K (in contrast to $\Delta = 35$ K and $\gamma = 64$ K in Fig. 3.2). Notice the greater scale for the magnetic energy $b$ .	72

## List of Abbreviations

AF	Anti-Ferromagnetic or Anti-Ferromagnetism
BCS	Bardeen, Cooper, and Schrieffer
CGS	Centimeter-gram-second
FM	Ferromagnetic or Ferromagnetism
HO	Hidden Order
PKE	Polar Kerr Effect
SI	International System
TR	Time-Reversal
TRS	Time-Reversal Symmetry
TRSB	Time-Reversal Symmetry Breaking
VMP	Vertical Mirror Plane

## Chapter 1: Background

This chapter provides a brief background on time-reversal symmetry breaking superconductors as they relate to the projects presented in the following chapters of the thesis.

### 1.1 Phenomenological Superconductivity

Superconductivity is a state of perfect conductivity in which electrical current can flow forever without resistance. Some metallic systems can reach this state by being cooled below a critical temperature  $T_c$ . When the temperature of a metal falls below its  $T_c$ , it undergoes a second order phase transition and its resistivity suddenly drops from a finite value to zero.

This phenomenon was first seen by H. Kamerlingh Onnes shortly after he invented liquid helium refrigeration in 1911 [2] and began using it to study other materials at low temperatures. In particular, Ohnes measured the low temperature resistance of mercury and found that below a temperature of 4K the material entered the state of zero resistance.

Almost two decades later in 1933, Meissner and Ochsenfeld discovered that in addition to perfect conductivity, superconductors display perfect diamagnetism

[3]. During the phase transition to superconductivity, magnetic flux through thick samples would be completely expelled. Perfect superconductivity only explains the resistance to a change in magnetic flux through a sample, but not the expulsion of magnetic flux. Both the perfect conductivity and the perfect diamagnetism of superconductors were explained phenomenologically in 1935 by the London brothers.

The London brothers proposed two phenomenological equations relating a superconductor's current density  $\mathbf{j}$  to the electric field  $\mathbf{E}$  and magnetic field  $\mathbf{B}$ ,

$$\frac{\partial \mathbf{j}}{\partial t} = \frac{1}{\Lambda} \mathbf{E} \quad (1.1)$$

$$\nabla \times \mathbf{j} = -\frac{1}{\Lambda c} \mathbf{B} \quad (1.2)$$

where

$$\Lambda = \frac{m}{n_s e^2} = \frac{\lambda_L^2}{c^2} \quad (1.3)$$

is a phenomenological parameter related to the density of supercharge carriers  $n_s$ , the electron charge  $e$ , the effective mass of supercharge carriers  $m$ , the speed of light  $c$ , and a London length scale  $\lambda_L$ . The first London equation (1.1) predicts perfect conductivity and the second London equation predicts perfect diamagnetism (1.2). The perfect conductivity can be seen by replacing the current density  $\mathbf{j}$  with the average charge carrier velocity  $\mathbf{v}$  using the definition of current density,  $\mathbf{j} = n_s e \mathbf{v}$ . In this case, equation (1.1) gives free acceleration according to Newton's Second

Law without any friction term,

$$m \frac{d\mathbf{v}}{dt} = e\mathbf{E}. \quad (1.4)$$

Meanwhile, perfect diamagnetism can be seen by combining the second London relation (1.2) with Ampere's Law,

$$\nabla \times \mathbf{B} = \frac{4\pi}{c} \mathbf{j} + \frac{1}{c} \frac{\partial E}{\partial t}, \quad (1.5)$$

to obtain

$$\nabla^2 \mathbf{B} = \frac{1}{\lambda^2} \mathbf{B}. \quad (1.6)$$

This Helmholtz differential equation predicts the exponential decay of  $\mathbf{B}$  on the length scale  $\lambda$  from  $\mathbf{B}$ 's value at the surface of the superconductor and thus describes the Meissner screening of the magnetic field from the bulk of a large superconducting sample. The London equations therefore explain the electrodynamic properties of superconductors. However, they do not explain these properties' microscopic origin.

It is worth noting that Fritz London argued that both of the London equations may follow from a quantum mechanical condition on the quantum mechanical ground state  $|\Psi_0\rangle$  of the superconductor. In terms of the canonical momentum of an electric particle,  $\hat{\mathbf{p}} = m\hat{\mathbf{v}} + e\mathbf{A}$ , which incorporates the vector potential  $\mathbf{A}$ , the

ground state condition is for the total momentum to be zero:

$$\langle \Psi_0 | \hat{\mathbf{p}} | \Psi_0 \rangle = \langle \Psi_0 | m\hat{\mathbf{v}} + e\mathbf{A} | \Psi_0 \rangle = 0. \quad (1.7)$$

In this case, the supercurrent  $\mathbf{j} = n_s e \langle \hat{\mathbf{v}} \rangle$  satisfies

$$\mathbf{j} = -\frac{n_s e^2}{m} \mathbf{A}. \quad (1.8)$$

The two London equations (1.1) and (1.2) can be derived from this last expression, but only in the Coulomb gauge.

The microscopic mechanism of superconductivity was discovered in 1956 by Leon Cooper [4]. He argued that the exclusion principle and Coulomb screening made it possible for electrons to have a net attractive interaction, which makes the electron gas unstable to the pairing of electrons. We can understand this instability in terms of the quantum field theory of fermionic annihilation operators  $\hat{\psi}_\sigma(\mathbf{k})$ , corresponding to electrons of momentum  $\mathbf{k}$  and spin  $\sigma$ . If there is an attractive effective interaction between electrons given by

$$\hat{H}_{int} = \int d^3\mathbf{k} g^{\sigma\sigma'}(\mathbf{k}) \hat{\psi}_\sigma^\dagger(\mathbf{k}) \hat{\psi}_{\sigma'}^\dagger(-\mathbf{k}) \hat{\psi}_\sigma(\mathbf{k}) \hat{\psi}_{\sigma'}(-\mathbf{k}), \quad (1.9)$$

then the system of electrons will possess a resonance that makes it unstable to a perturbation of the form

$$\hat{H}_p = \int d^3\mathbf{k} \left[ \Delta^{\sigma\sigma'}(\mathbf{k}) \hat{\psi}_\sigma^\dagger(\mathbf{k}) \hat{\psi}_{\sigma'}^\dagger(-\mathbf{k}) + \Delta^{\dagger\sigma\sigma'}(\mathbf{k}) \hat{\psi}_\sigma(\mathbf{k}) \hat{\psi}_{\sigma'}(-\mathbf{k}) \right] \quad (1.10)$$

below a particular temperature  $T_c$ , which can be computed diagrammatically. The effective interaction (1.9) has the  $U(1)$  gauge symmetry typical of electrons,

$$\hat{\psi}_\sigma \rightarrow e^{-i\phi} \hat{\psi}_\sigma, \quad \hat{\psi}_\sigma^\dagger \rightarrow e^{i\phi} \hat{\psi}_\sigma^\dagger. \quad (1.11)$$

However, if Cooper pairing occurs, then there is an anomalous average which breaks this symmetry,

$$\Delta^{\sigma\sigma'}(\mathbf{k}) = g^{\sigma\sigma'}(\mathbf{k}) \langle \hat{\psi}_\sigma(\mathbf{k}) \hat{\psi}_{\sigma'}(-\mathbf{k}) \rangle. \quad (1.12)$$

The mean-field  $\Delta^{\sigma\sigma'}(\mathbf{k})$  is known as the superconducting gap and is an order parameter for superconductivity. Since the only gauge transformations that preserve the gap are multiplication by 1 and  $-1$ , we say that superconductivity has  $U(1) \rightarrow \mathbb{Z}_2$  symmetry breaking. If  $\Delta^{\sigma\sigma'}(\mathbf{k})$  breaks additional symmetries other than the  $U(1)$  gauge symmetry, then we say the superconductivity is unconventional.

After the discovery of Cooper pairing, Schrieffer constructed the many-body wavefunction for the superconducting ground state and shortly afterwards a full theory of superconductivity was presented by Bardeen, Cooper, and Schrieffer (BCS) in 1957 [5]. The BCS theory assumes a simple spin-singlet Cooper pairing,

$$\Delta(\mathbf{k}) = g \langle \hat{\psi}_\uparrow(\mathbf{k}) \hat{\psi}_\downarrow(-\mathbf{k}) \rangle + g \langle \hat{\psi}_\downarrow(\mathbf{k}) \hat{\psi}_\uparrow(-\mathbf{k}) \rangle. \quad (1.13)$$

This allows us to admit a mean-field approximation that replaces the quartic interaction term in (1.9) with a quadratic mean-field interaction like the one in (1.10),

to obtain

$$\hat{H}_{\text{MF}} = \int d^3\mathbf{k} \left[ \hat{\psi}_\sigma^\dagger(\mathbf{k}) \epsilon_{\mathbf{k}}^\sigma \hat{\psi}_\sigma(\mathbf{k}) + \Delta \hat{\psi}_\uparrow^\dagger(\mathbf{k}) \hat{\psi}_\downarrow^\dagger(-\mathbf{k}) + \Delta^* \hat{\psi}_\downarrow(-\mathbf{k}) \hat{\psi}_\uparrow(\mathbf{k}) - \frac{|\Delta|^2}{g} \right] \quad (1.14)$$

where  $\epsilon_{\mathbf{k}}^\sigma$  gives the kinetic energy of an electron with spin  $\sigma$  and momentum  $\mathbf{k}$ . The mean-field theory of (1.14) can be used to derive the BCS theory of superconductivity and describes conventional superconductors, also referred to as s-wave superconductors. Everything seemed well-understood in terms of BCS theory until the discovery in 1986 of high-temperature superconductors and unconventional superconductivity [6].

The era of unconventional superconductivity began with Anderson and Morel investigating superconducting phases that would later be known as the *A*- and *B*- phases in superfluid  $^3\text{He}$  [7]. In contrast with conventional s-wave superconductors, the *A*- and *B*- phases are characterized by angular momentum  $L = 1$  and spin-triplet configurations. Although unconventional pairing was studied both theoretically and in heavy Fermion compounds in the early 80s [8], the concept did not become widely popular until the 1986 discovery of high-temperature superconductivity in cuprates.

The unexpected discovery of high- $T_c$  superconductivity in cuprates such as  $\text{La}_2\text{CuO}_4$  and  $\text{Sr}_2\text{CuO}_4$  led to the eventual discovery by Yoshiteru Maeno and collaborators of an analog superconductor  $\text{Sr}_2\text{RuO}_4$  in 1994 [9]. This superconductor drew immediate interest because it has the same perovskite structure as  $\text{La}_2\text{CuO}_4$  and  $\text{Sr}_2\text{CuO}_4$ , but is not a cuprate. Soon after the discovery of  $\text{Sr}_2\text{RuO}_4$ , it was pro-



posed that this material had p-wave and spin-triplet pairing based on its similarity to  $^3\text{He}$  and closely related ferromagnetic compounds such as  $\text{SrRuO}_3$  [10]. Muon spin resonance experiments eventually found that  $\text{Sr}_2\text{RuO}_4$  breaks time-reversal symmetry (TRS) [11].

## 1.2 Time-Reversal Symmetry Breaking

The question of broken TRS has a special place in the study of superconducting systems, because TRS is a property of conventional s-wave superconductivity and has multiple implications that are violated in interesting unconventional superconductors. TRS refers to the preservation of physical observables under a time-reversal (TR) operator that exchanges physical time with its opposite,  $\mathbb{T} : t \rightarrow -t$ . In classical physics, time-reversal amounts to changing the sign of quantities with an odd dependence on the sign of the time parameter, such as velocity or angular momentum. In quantum physics, time-reversal is represented by an antiunitary operator which has the action  $\langle \mathbb{T}\psi | \mathbb{T}\phi \rangle = \langle \phi | bra \rangle$ . Additionally, due to Fermi statistics, time-reversal must also have a non-trivial exchange operation on fermionic operators,

$$\mathbb{T} : \hat{\psi}_\uparrow \rightarrow -\hat{\psi}_\downarrow^\dagger \quad (1.15)$$

$$\mathbb{T} : \hat{\psi}_\downarrow \rightarrow \hat{\psi}_\uparrow^\dagger. \quad (1.16)$$

The BCS mean-field Hamiltonian in equation (1.14) is invariant under application of  $\mathbb{T}$ , so the dynamics of the system are time-reversal symmetric. On the

other hand the Hamiltonian for a spin-triplet (p-wave) superconductor

$$\hat{H}_P = \sum_k c_{\uparrow}^{\dagger} c_{\uparrow} + \Delta(k) c_{\uparrow}^{\dagger} c_{\uparrow}^{\dagger} + \Delta^*(k) c_{\uparrow} c_{\uparrow} \quad (1.17)$$

clearly is not preserved by TR, since  $\mathbb{T}$  inverts all of the spins.

One important consequence of TRS is that conventional superconductors can be surprisingly dirty. Philip Anderson showed that if a Cooper pair is formed between an electron and its exact time-reverse counterpart, then the system will be immune to scattering from non-magnetic (or TRS respecting) impurities [12]. A significant fraction of chemical centers in a conventional superconductor can be impurities without significant modification of the transition temperature  $T_c$ . Since this is no longer the case in TRS breaking (TRSB) superconductors, impurity scattering can actually be used to study deviations from conventional superconductivity. For example, it has been seen that superconductivity is suppressed by increasing the number of non-magnetic impurities in  $\text{Sr}_2\text{RuO}_4$  [13].

Another consequence of TRS more directly related to the work in this thesis is the impossibility of transverse Hall conductivity in a system that has TRS. This follows from the Onsager-Casimir relation for conductivity tensor [14]

$$\sigma(B) = \sigma^T(-B), \quad (1.18)$$

which guarantees that the conductivity tensor  $\sigma$  is symmetric unless there is an applied magnetic field  $B \neq 0$ . The symmetric part of the conductivity can be

diagonalized by a choice of coordinates, so an anti-symmetric part of the conductivity tensor is necessary for transverse Hall conductivity  $\sigma_H$ . Therefore, if a system has intrinsic Hall conductivity (in the absence of an applied magnetic field), it must break time-reversal symmetry. Consonant with this result, some theoretical TRSB systems are predicted to have an anomalous Hall effect [15, 16].

A superconductor which breaks TRS cannot be an s-wave superconductor, and so by definition it belongs to the open category of unconventional superconductors. It is therefore worthwhile to search for TRSB superconductors, because they will have interesting pairing mechanisms. We can do this by looking for systems which have anomalous Hall conductivity detectable through experiment. So far a handful of materials have been found to break TRS, and it is possible that each of these materials is a chiral superconductor.

### 1.3 Magneto-Optical Polar Kerr Effect

A direct probe of time-reversal (TR) symmetry (TRS) has been constructed based on the magneto-optical polar Kerr effect (PKE). If a material breaks TRS then it is possible for there to be a small Kerr angle  $\theta_K$  of rotation between the incoming beam and outgoing beam. Experiments carried out by Xia et al., which identified TRS-breaking (TRSB) in several superconductors, were done with a zero-area Sagnac interferometer [17, 18].

The basic premise of using a Sagnac interferometer is that a beam of light and its reciprocal under TR follow the same path closed but in opposite directions as

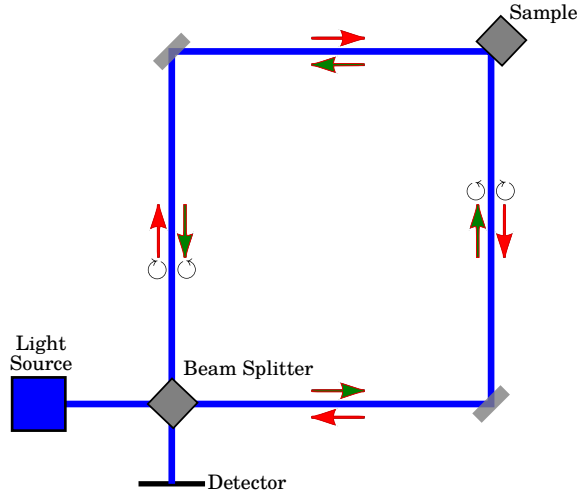


Figure 1.1: Schematic diagram of a simplified Sagnac interferometer in which a beam and its reciprocal under time-reversal interact with a sample and then interfere at the detector. Since the beam paths are reciprocal with respect to time-reversal, only a time-reversal symmetry breaking sample produces a signal. (Credit: This figure was modified from a freely available Creative Commons image owned by Wikipedia user Krishnavedala.)

in Fig. 1.1. A phase shift between the beam and its reciprocal then indicates the presence of some non-reciprocal or TRSB effect during the path of the light, since otherwise TRS implies the two beams will be treated equivalently. However, since a Sagnac interferometer is known to display an unrelated phase shift proportional to area, the actual interferometers used to measure PKE use no area - the branches of the interferometer are the vertical and horizontal modes of a waveguide occupying the same physical space. Additionally, the vertical and horizontal modes of the waveguide have different propagation speeds for light, allowing the two reciprocal beams to interact with the sample separately. The interpretation of a phase shift in this interferometer arising from TRSB is associated with the Reciprocity Theorem by Alexander Fried.

The Reciprocity Theorem is a generalization of the Onsager-Casimir relation

discussed above. It shows that, if TRS is respected, then no Kerr rotation is permitted in a material [19]. It is shown that for small perturbations, the Feynman propagator  $G_{++}^F$  for positively circularly polarized light traveling from  $\mathbf{r}_1 \rightarrow \mathbf{r}_2$ , is identical to the Feynman propagator  $G_{--}^F$  for negatively polarized light traveling from  $\mathbf{r}_2 \rightarrow \mathbf{r}_1$ ,

$$G_{++}^F(t_2, \mathbf{r}_2, t_1, \mathbf{r}_1) = G_{--}^F(t_2, \mathbf{r}_1, t_1, \mathbf{r}_2). \quad (1.19)$$

The propagator  $G_{\mu\nu}^F$  is given in terms of the ground state of the material  $|g\rangle$  and the time-ordered product of vector potential field operators  $\hat{A}_\mu(\mathbf{r}, t)$ ,

$$G_{\mu\nu}^F(t_2, \mathbf{r}_2, t_1, \mathbf{r}_1) = \langle g | T[\hat{A}_\mu(\mathbf{r}_2, t_2)\hat{A}_\nu(\mathbf{r}_1, t_1)] | g \rangle. \quad (1.20)$$

The result follows from the TR behavior of the Hamiltonian  $\hat{H} \rightarrow \hat{H}$ , the time-evolution operator  $\exp(-i\hat{H}t) \rightarrow \exp(i\hat{H}t)$ , and the ground state  $|g\rangle \rightarrow |Tg\rangle^*$  of the TRS system. Since  $\mathbb{T}$  is anti-unitary, it takes the ground state to the complex conjugate and time-reversed state  $|Tg\rangle^*$ , where  $\langle v |^* | u \rangle^* = \langle u | v \rangle$ . Under TR the vector potential obeys:

$$A_\mu(t, \mathbf{r}) \rightarrow \mathbb{T} \exp(i\hat{H}t) A_\mu(0, \mathbf{r}) \exp(-i\hat{H}t) \mathbb{T}^\dagger \quad (1.21)$$

$$= \mathbb{T} \exp(i\hat{H}t) \mathbb{T}^\dagger \mathbb{T} A_\mu(0, \mathbf{r}) \mathbb{T}^\dagger \mathbb{T} \exp(-i\hat{H}t) \mathbb{T}^\dagger \quad (1.22)$$

$$= -\exp(i\hat{H}t) A_\mu(0, \mathbf{r}) \exp(-i\hat{H}t) = -A_\mu(-t, \mathbf{r}). \quad (1.23)$$

Then one can show Eq. (1.19) by basic time-reversal using the following series of equalities:

$$G_{\mu\nu}^F(t_2, \mathbf{r}_2, t_1, \mathbf{r}_1) = \langle g | T[\hat{A}_\mu(\mathbf{r}_2, t_2)\hat{A}_\mu(\mathbf{r}_1, t_1)] | g \rangle \quad (1.24)$$

$$= \langle g | \mathbb{T}^\dagger T[\mathbb{T}\hat{A}_\mu(\mathbf{r}_2, t_2)\mathbb{T}^\dagger\mathbb{T}\hat{A}_\nu(\mathbf{r}_1, t_1)\mathbb{T}^\dagger] \mathbb{T} | g \rangle \quad (1.25)$$

$$= \langle \mathbb{T}g |^* T[\hat{A}_\mu(\mathbf{r}_2, -t_2)\hat{A}_\nu(\mathbf{r}_1, -t_1)] | \mathbb{T}g \rangle^* \quad (1.26)$$

$$= \langle \mathbb{T}g | T[\hat{A}_\nu(\mathbf{r}_2, -t_1)\hat{A}_\mu(\mathbf{r}_1, -t_2)] | \mathbb{T}g \rangle \quad (1.27)$$

$$= \langle \mathbb{T}g | T[\hat{A}_\nu(\mathbf{r}_2, t_2)\hat{A}_\mu(\mathbf{r}_1, t_1)] | \mathbb{T}g \rangle \quad (1.28)$$

$$= \langle g | T[\hat{A}_\nu(\mathbf{r}_2, t_2)\hat{A}_\mu(\mathbf{r}_1, t_1)] | g \rangle \quad (1.29)$$

$$= G_{\nu\mu}^F(t_2, \mathbf{r}_1, t_1, \mathbf{r}_2). \quad (1.30)$$

The Eq. (1.28) was reached using time-translation symmetry and Eq. (1.29) was reached using the TRS of the ground state  $|\mathbb{T}g\rangle = |g\rangle$ . From the symmetry in equation (1.19), it follows that the Kerr rotation in the phase of circularly polarized light is zero:

$$\theta_K = \frac{1}{2}\arg G_{++}(t_2, \mathbf{r}_2, t_1, \mathbf{r}_1) - \frac{1}{2}\arg G_{--}(t_2, \mathbf{r}_1, t_1, \mathbf{r}_2) = 0. \quad (1.31)$$

The Reciprocity Theorem provides support for the interpretation of the Kerr effect as evidence of microscopic TRSB.

The zero-area Sagnac interferometer has been used to detect a small but clearly discernible Kerr signal in several chiral superconductors:  $\text{Sr}_2\text{RuO}_4$  [20],  $\text{UPt}_3$  [21],  $\text{URu}_2\text{Si}_2$  [22],  $\text{PrOs}_4\text{Sb}_{12}$  [23], and Bi/Ni bilayers [24]. The response tends to be

on the order of nanoradians, which agrees with subsequent theoretical calculations [25, 26] that give  $\theta_K$  in terms of the imaginary part of the Hall conductivity  $\sigma_H''$ ,

$$\theta_K \approx \frac{4\pi}{\omega} \frac{\sigma_H''}{n(n^2 - 1)} \approx 10^{-8} \frac{\Delta^2}{T_c^2} \text{ rad.} \quad (1.32)$$

Here  $n$  is the index of refraction in a TRSB sample,  $\omega \approx 239$  THz is the frequency of light used to probe the PKE, and  $\Delta$  is the superconducting gap. In these TRSB superconductor systems, the Kerr angle is proportional to Hall conductivity, and so the anomalous Hall effect should be possible in these systems in addition to the Kerr effect. In the next chapter we explore the possibility of measuring the anomalous Hall conductivity directly.

## Chapter 2: The Hall Effect as a Probe of Time-Reversal Symmetry Breaking in Superconductors

### 2.1 Introduction

Chiral superconductivity breaks time-reversal symmetry and is regarded as desirable since it may enable quantum information processing [16, 27, 28]. One experimental probe of chiral superconductivity looks for time-reversal symmetry breaking through non-zero ac Hall conductivity. The existence of ac Hall conductivity implies a Magneto-optical Kerr effect (MOKE) that has been seen in several superconducting systems:  $\text{Sr}_2\text{RuO}_4$  [20],  $\text{UPt}_3$  [21],  $\text{URu}_2\text{Si}_2$  [22],  $\text{PrOs}_4\text{Sb}_{12}$ , and Bi/Ni bilayers [24]. Despite the success of these MOKE experiments, they have some limitations. The MOKE probes the surface of a material, rather than its bulk, and it produces only a small signal. Also, the photons used to detect the MOKE have a much higher energy than the superconducting gap ( $\hbar\omega \gg \Delta, kT_c$ ). These MOKE measurements leave open the question of time-reversal symmetry at low frequency in the bulk of a superconductor. This chapter therefore proposes an alternative and low-frequency experiment capable of observing anomalous dc Hall conductivity  $\sigma_H$  directly.



Although time-reversal symmetry breaking implies an anomalous dc Hall conductivity, it is controversial whether this effect appears in superconductors [?]. Since resistivity is the inverse of conductivity,  $\rho = \sigma^{-1}$ , the experimental observation of zero transverse resistivity  $\rho_{xy} = 0$  is often taken to indicate zero transverse conductivity  $\sigma_{xy} = \sigma_H = 0$ . However,  $\rho_{xy}$  and  $\sigma_H$  can be zero independently [29] since  $\rho_{xy} = \sigma_H / (\sigma_{xx}\sigma_{yy} + \sigma_H^2)$  with  $\sigma_{xx} \rightarrow \infty$ . It is further difficult to measure bulk Hall conductivity using the typical bar geometry, because supercurrent shunts Hall current in the bulk and both bulk and edge states may carry current. Since it is difficult to observe the Hall effect in the bar geometry, we consider a low-frequency Hall effect experiment in a geometry where the symmetry is more favorable to distinguishing the effect.

One of the early Hall effect measurements was by Von Corbino in a thin cylindrical annulus called a Corbino disk [30]. We consider a qualitatively similar infinitely long cylindrical annulus placed inside an axial time-varying magnetic field. The applied magnetic field induces a circular electric field  $E_\theta$  which in turn produces a Hall radial Hall current  $j_r^H = \sigma_H E_\theta$ . We find that a surface charge oscillation occurs at the outer boundary of the cylinder which corresponds to a radial potential difference  $V_r^H$  between the inner and outer radii of the cylinder. Due to axial symmetry, the charge oscillation effect can only result from the transverse Hall conductivity.

We calculate the linear response of oscillating surface charge and propose a contactless measurement of  $V_r^H$  using a modified coaxial cable. Numeric predictions of the surface charge and potential difference are given in terms of  $\sigma_H$  estimated

from a particular microscopic theory of TRSB d-wave superconductivity [16]. We also compare our result with Hall conductivity resulting from the external magnetic field and find that only intrinsic Hall conductivity gives rise to a linear response at frequency of the applied magnetic field.

## 2.2 Electrodynamics of Superconductors

Let us review the relevant electrodynamic equations. We will assume the axis of magnetization in the TRSB superconductor is oriented along the z-axis, so that any Hall effect is in the  $x, y$ -plane. Maxwell's equations describe the electric field  $\mathbf{E}$ , the magnetic field  $\mathbf{B}$ , supercurrent density  $\mathbf{j}^S$ , transverse Hall current density  $\mathbf{j}^H$ , and bulk charge density  $\rho$  (in cgs units),

$$\nabla \cdot \mathbf{E} = 4\pi\rho, \quad \nabla \cdot \mathbf{B} = 0, \quad (2.1)$$

$$\nabla \times \mathbf{E} = -\frac{1}{c} \frac{\partial \mathbf{B}}{\partial t}, \quad (2.2)$$

$$\nabla \times \mathbf{B} = \frac{4\pi}{c} (\mathbf{j}^S + \mathbf{j}^H) + \frac{1}{c} \frac{\partial \mathbf{E}}{\partial t}. \quad (2.3)$$

In the Coulomb gauge, the supercurrent density  $\mathbf{j}^S$  is generally given in terms of the vector potential  $\mathbf{A}$  and the local superfluid phase  $\phi$ ,

$$\mathbf{j}^S = -\frac{n_s e^2}{mc} \left( \mathbf{A} - \frac{\hbar}{2e} \nabla \phi \right). \quad (2.4)$$

We assume  $\nabla \phi = 0$  because we are working in the linear response regime of small fields in which vortices are not created at any time. The expression for supercurrent

in Eq. (2.4) gives us the London equations relating supercurrent density to the electric and magnetic fields,

$$\frac{\partial \mathbf{j}^S}{\partial t} = \frac{n_s e^2}{m} \mathbf{E}, \quad (2.5)$$

$$\nabla \times \mathbf{j}^S = -\frac{n_s e^2}{mc} \mathbf{B}. \quad (2.6)$$

The Hall current density  $\mathbf{j}^H$  is given in terms of the anomalous Hall conductivity  $\sigma_H$ ,

$$\mathbf{j}^H = \sigma_H \mathbf{E} \times \hat{\mathbf{z}}. \quad (2.7)$$

In a conventional superconductor ( $\sigma_H = 0$ ), taking the curl of Ampere's Law and using the second London equation (2.6) gives a differential equation for Meissner screening of the magnetic field,

$$\nabla^2 \mathbf{B} = \frac{4\pi n_s e^2}{mc^2} \mathbf{B}. \quad (2.8)$$

The coefficient of proportionality in the Meissner screening equation gives a temperature-dependent ( $T$ ) frequency  $\omega_L$  and length scale  $\lambda_L$  related as

$$\omega_L(T) = \frac{c}{\lambda_L} = \sqrt{\frac{4\pi n_s(T) e^2}{m}}. \quad (2.9)$$

This London frequency  $\omega_L$  is the characteristic timescale over which supercharge responds to perturbation and  $\lambda_L$  is the length scale over which the electromagnetic

field exponentially decays into the bulk of a superconductor. At finite temperature  $T \neq 0$ , the number of supercharge carriers  $n_s(T)$  is less than the total number of charge carriers  $n$ , and so the London frequency  $\omega_L(T)$  is less than the plasma frequency,

$$\omega_p = \sqrt{\frac{4\pi n e^2}{m}}, \quad (2.10)$$

in general. However, the London frequency approaches the plasma frequency ( $\omega_L \rightarrow \omega_p$ ) only in the clean limit  $T \rightarrow 0$ .

### 2.3 AC Meissner Screening for $\sigma_H = 0$

In place of the Corbino disk of finite thickness, we consider an infinitely long annular cylinder of inner radius  $R_i$  and outer radius  $R_o$  placed coaxially inside a larger solenoid of radius  $R_s > R_o$ . This qualitatively similar, but mathematically simpler system is depicted in figure [2.1](#).

We have a cylindrical system with coordinates  $\mathbf{x} = (r, \theta, z)$  in which an axial magnetic field induces circular electric field and supercurrent. For simplicity, we assume the applied magnetic field of the solenoid  $\mathbf{B}_s(t) = B_0 \sin(\omega t) \hat{z}$ , which is valid in the low frequency approximation,

$$\omega \ll c/R_s. \quad (2.11)$$

Consequently, the boundary condition for the magnetic field inside the cylinder will

be continuity with the uniform field of the solenoid,

$$\mathbf{B}_s(t) = \mathbf{B}(r = R_o, t) = B_0 e^{-i\omega t} \hat{\mathbf{z}}. \quad (2.12)$$

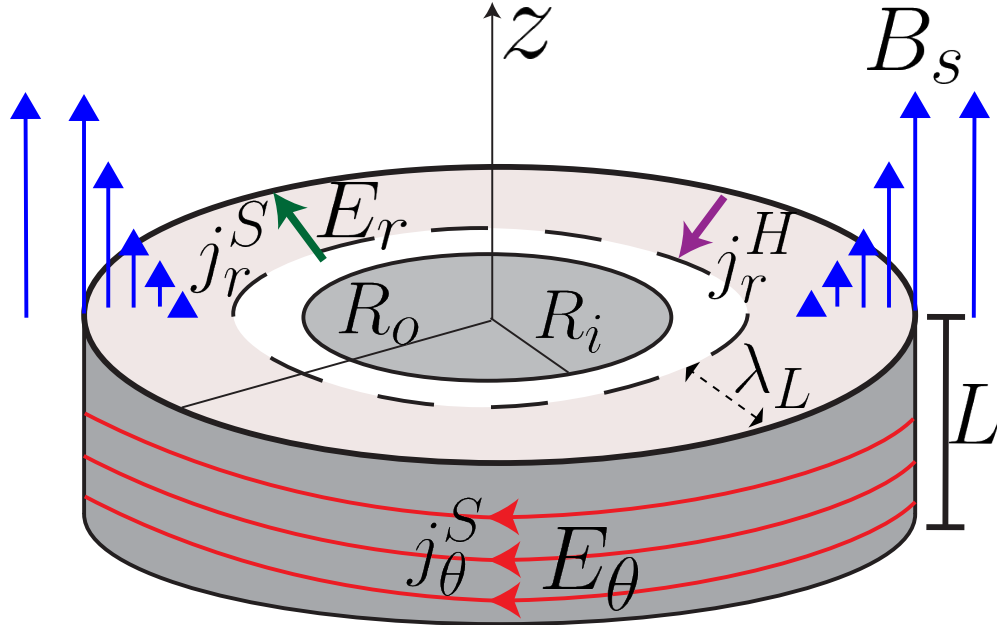


Figure 2.1: Our setup consists of a superconducting cylinder of inner radius  $R_i$ , outer radius  $R_o$  and length  $L$ . Most effects occur near the outer edge of the superconductor.

We treat the superconducting system perturbatively in  $\sigma_H$  by first finding the electromagnetic response of a normal superconductor ( $\sigma_H = 0$ ) to the applied magnetic field  $\mathbf{B}_0(t)$  and then by showing that surface charge density oscillations occur at the outer edge of the superconductor for  $\sigma_H \neq 0$ . We begin by writing Maxwell's equations in the superconducting region ( $R_i < r < R_o$ ) in the frequency domain for  $\sigma_H = 0$ . In the frequency domain, Faraday's Law (2.2) is given by

$$\nabla \times \mathbf{E} = \frac{i\omega}{c} \mathbf{B}. \quad (2.13)$$

In Ampere's Law (2.3) with  $\sigma_H = 0$ , we replace  $\mathbf{j}^S$  using the first London relation (2.5) to obtain

$$\nabla \times \mathbf{B} = -\frac{i\omega}{c} \left[ 1 - \frac{\omega_L^2}{\omega^2} \right] \mathbf{E}. \quad (2.14)$$

Since we are assuming an infinitely long system with cylindrical symmetry, the  $\theta$  and  $z$  derivatives vanish in equations (2.13) and (2.14). This simplification allows us to set  $B_r = 0$ ,  $B_\theta = 0$ ,  $E_r = 0$ , and  $E_z = 0$  while  $E_\theta$  and  $B_z$  satisfy the two coupled equations,

$$\frac{\partial E_\theta}{\partial r} + \frac{E_\theta}{r} = \frac{i\omega}{c} B_z \quad (2.15)$$

$$\frac{\partial B_z}{\partial r} = \frac{i\omega}{c} \left[ 1 - \frac{\omega_L^2}{\omega^2} \right] E_\theta. \quad (2.16)$$

Combining the equations for  $E_\theta$  and  $B_z$  (2.15) and (2.16) gives us modified Bessel differential equations in  $r$ ,

$$\frac{\partial^2 E_\theta}{\partial r^2} + \frac{1}{r} \frac{\partial E_\theta}{\partial r} - \frac{1}{r^2} E_\theta = \frac{\omega_L^2 - \omega^2}{c^2} E_\theta \quad (2.17)$$

$$\frac{\partial^2 B_z}{\partial r^2} + \frac{1}{r} \frac{\partial B_z}{\partial r} = \frac{\omega_L^2 - \omega^2}{c^2} B_z, \quad (2.18)$$

of order one and zero, respectively. Both Bessel equations have the same frequency-dependent length scale,

$$\lambda(\omega) = \sqrt{\frac{c^2}{\omega_L^2 - \omega^2}}, \quad (2.19)$$

which is the characteristic length scale for screening. In general, the modified Bessel equation of order  $n$  has two solutions,  $K_n$  and  $I_n$ , but we discard the solution  $K_n$  because it grows exponentially with decreasing radius and is non-zero in the bulk. Using the boundary condition in Eq. (2.12), we find the solution to (2.18) for magnetic field  $B_z$  for  $R_i < r < R_o$ ,

$$B_z(r) = B_0 \frac{I_0(r/\lambda(\omega))}{I_0(R_o/\lambda(\omega))}. \quad (2.20)$$

Substituting this expression for  $B_z(r)$  into Eq. (2.16) gives a corresponding electric field,

$$E_\theta(r) = \frac{\lambda(\omega)}{c} i\omega B_0 \frac{I_1(r/\lambda(\omega))}{I_0(R_o/\lambda(\omega))}. \quad (2.21)$$

We then make the low-frequency assumption

$$\omega \ll \omega_L, \quad (2.22)$$

in which case the screening length is approximately the London penetration depth  $\lambda(\omega) \approx \lambda_L$ . Assuming  $\lambda_L < R_s$ , the low-frequency limit in Eq. (2.22) is less restrictive than the low-frequency limit we assumed to avoid electromagnetic retardation in Eq. (2.11), so it follows naturally. In this limit, since  $r > R_i \gg \lambda_L$ , we can use the large-argument Bessel function approximation,  $I_n(z) \approx \exp(z)/\sqrt{2\pi z}$ , with

$z = r/\lambda(\omega) \gg 1$ , in Eq. (2.20) and Eq. (2.21), to obtain

$$B_z(r) \approx B_0 \sqrt{\frac{R_o}{r}} e^{(r-R_o)/\lambda(\omega)} \quad (2.23)$$

$$E_\theta(r) \approx i\omega B_0 \frac{\lambda(\omega)}{c} \sqrt{\frac{R_o}{r}} e^{(r-R_o)/\lambda(\omega)}. \quad (2.24)$$

In Eqns. (2.23) and (2.24), the electric and magnetic fields decay exponentially to a value of zero in the bulk. This is the Meissner effect, in which the magnetic field is shielded from the bulk of the superconductor.

The non-zero circular electric field in Eq. (2.24) corresponds to circular supercurrent that is shielding magnetic flux from the superconductor, given by:

$$j_\theta^S(r, \omega) = \frac{i\omega_L^2}{4\pi\omega} E_\theta \approx -\frac{\omega_L}{4\pi} B_0 \sqrt{\frac{R_o}{r}} e^{(r-R_o)/\lambda(\omega)}. \quad (2.25)$$

The supercurrent  $j_\theta^S$  flows near the outer surface of the superconductor and forms a surface current density  $I_{2D}^S$  of radius  $r \approx R_o$ , which we find by integrating in the radial direction

$$I_{2D}^S = \int_{R_i}^{R_o} j_\theta^S dr = -\frac{c}{4\pi} B_0. \quad (2.26)$$

From Ampere's Law, one can see that  $B_0 + 4\pi I_{2D}^S/c = 0$  implies the the magnetic field vanishes in the bulk ( $R_o - r \gg \lambda_L$ ) as expected.

So far, we have found the electromagnetic response of the Corbino disk to be the usual Meissner screening of magnetic field from the superconducting bulk via



supercurrent. As a consequence of  $\sigma_H = 0$ , we found there is no radial field  $E_r = 0$  and, obviously, no Hall current. This changes in the next section when we consider  $\sigma_H \neq 0$ .

## 2.4 Radial Charge Oscillation for $\sigma_H \neq 0$

Now suppose the superconducting annulus at  $R_i < r < R_o$  breaks time-reversal symmetry and has a non-zero Hall conductivity  $\sigma_H \neq 0$ . The immediate consequence from Eq. (2.7) is a radial Hall current given by

$$j_r^H(r) = \sigma_H E_\theta(r). \quad (2.27)$$

Since charge flows in the radial direction, it is possible for there to be a radial electric field  $E_r$  and a buildup of charge.

We may solve for  $E_r$  by considering the radial-component equation of Ampere's Law (2.3). The radial component of the curl in Eq. (2.3) vanishes due to symmetry, giving us a relationship between the charge and displacement currents. In the Fourier domain we have

$$\frac{i\omega}{c} E_r = \frac{4\pi}{c} (j_r^S + j_r^H) = \frac{\omega_L^2}{c\omega} E_r + \frac{4\pi\sigma_H}{c} E_\theta. \quad (2.28)$$

We solve for  $E_r$  to find

$$E_r(r, \omega) = i \frac{4\pi\sigma_H \omega c^2}{\omega_L^2 - \omega^2} E_\theta(r, \omega). \quad (2.29)$$

The radial electric field is proportional to the radially screened circular electric field.

The radial electric field can only exist at the boundary of the charge-neutral superconductor if there is a surface charge density  $q$  as required by Gauss' Law,

$$q = -\frac{1}{4\pi}E_r(R_o, \omega). \quad (2.30)$$

We consider this surface charge density to be located entirely at the surface because the Thomas-Fermi distance over which it is spread is much smaller than the London penetration depth. The surface charge  $q$  is also necessary to balance the radial current leaving the bulk of the superconductor. Using our expression for  $E_r$  from Eq. (2.29) in Eq. (2.30) we find

$$q(\omega) = \frac{\sigma_H \omega^2}{(\omega_L^2 - \omega^2)^{3/2}} B_0 \frac{I_1(R_o/\lambda(\omega))}{I_0(R_o/\lambda(\omega))}. \quad (2.31)$$

The surface charge density indicates an oscillator with resonant frequency  $\omega_L$  which is driven by the external magnetic field  $B_0$ .

The surface charge density at the outer edge of the cylinder is compensated by a bulk charge density  $\rho$ . From Gauss' Law we have

$$\rho = \frac{1}{4\pi} \nabla \cdot \mathbf{E} = \frac{1}{r} \frac{\partial}{\partial r} (r E_r). \quad (2.32)$$

Substituting using Eqs. (2.29) and (2.21), we find

$$\rho = -\frac{\sigma_H \omega^2 c}{\omega_L^2 - \omega^2} B_0 \frac{I_0(r/\lambda(\omega))}{I_0(R_o/\lambda(\omega))}. \quad (2.33)$$

The charge density is largest near the surface and exponentially decays into the bulk over the London screening distance, and the bulk charge density is proportional to the shielded magnetic field in Eq. (2.20). Integrating the bulk charge density over the volume of the annular cylinder gives a charge opposite to the charge on the outer surface:  $2\pi L \int_{R_i}^{R_o} \rho(r)rdr = -2\pi LR_oq$ .

The surface charge  $q$  also results in a radial potential difference between the inner and outer surfaces of the superconductor,

$$V_r^H = - \int_{R_i}^{R_o} E_r dr = \frac{4\pi\sigma_H\omega^2 c}{(\omega_L^2 - \omega^2)^2} B_0. \quad (2.34)$$

Using our assumption  $\omega \ll \omega_L$ , we have  $\lambda(\omega) \rightarrow \lambda_L$ , so we can repeat the exponential approximation for the Bessel functions used in Eq. (2.24) for Eqs. (2.31) and (2.34) to obtain the approximations

$$q(\omega) \approx \frac{\sigma_H\omega^2}{\omega_L^3} B_0, \quad (2.35)$$

$$V_r^H \approx \frac{4\pi\sigma_H\omega^2 c}{\omega_L^4} B_0. \quad (2.36)$$

We will estimate these values in the next section.

Aside from the radial current and oscillation of charge, which are first-order in  $\sigma_H$ , there is a second-order correction to the circular current from the Hall current in Eq. (2.7),

$$j_\theta^H = -\sigma_H E_r(r) \approx -i \frac{4\pi\sigma_H^2\omega}{\omega_L^2} E_\theta(r). \quad (2.37)$$

However, the Hall contribution to circular current in Eq. (2.37) is negligible compared to the circular supercurrent in Eq. (2.25),  $j_\theta^H \ll j_\theta^S$ , assuming that

$$\sigma_H^2 \ll \frac{\omega_L^4}{\omega^2}, \quad (2.38)$$

which is the case based on our estimate in the next section. Note that in Gaussian units,  $\sigma_H$  has units of frequency.

## 2.5 Estimating the Hall Conductivity

In this section we estimate the magnitude of the 3D Hall conductivity  $\sigma_H = \sigma_H^{3D}$  in order to estimate the strength of the superconducting Hall effect in the previous section. To do this, we relate the 3D Hall conductivity used in our calculation to the 2D Hall conductivity previously calculated for multi-band TRSB superconducting systems [15, 16, 31]. For  $n$  layers of material of height  $L$ , the 3D Hall conductivity and 2D Hall conductivity are related in the following way:

$$L\sigma_H^{3D} = n\sigma_H^{2D}. \quad (2.39)$$

Using Eq. (31) of Ref. 16 (with  $\omega = 0$ ) we find an estimate of the 2D Hall conductivity in terms of the chemical potential  $\mu$ , superconducting gap  $\Delta$ , and a numeric factor  $F$ ,

$$\sigma_H^{2D}(\omega) = \frac{e^2 \mu}{h t} \left( \frac{\Delta}{t} \right)^2 F \quad (2.40)$$

in units of a hopping energy  $t$ . The numeric factor  $F$  is given by

$$F = -48\pi t^5 \int_{BZ} d^2k \frac{\sin^2(\frac{\sqrt{3}}{2}k_y) \left( \cos(\frac{3}{2}k_y) - \cos(\frac{\sqrt{3}}{2}k_x) \right)^2}{E_{1,k}E_{2,k}(E_{1,k} + E_{2,k})^3}. \quad (2.41)$$

This numeric factor can be estimated analytically as a consequence of  $E_{2,k}$  dominating the integral near the K and K' points where  $\Delta \ll E_{2,k} \approx -\Delta - v \cdot k \ll t$ . Near these points, it is the case that

$$F \propto - \int_{\Delta}^t \frac{d|k|}{|k|} = c \log(\Delta/t), \quad (2.42)$$

where  $c$  is a band-structure-dependent constant. We use this estimate in the following section.

The specific form of Eq. (2.41) is calculated as follows. Setting  $\omega = 0$  in Eq. (31) of Ref. 16 gives a Masubara sum over the frequencies  $v_m = 2\pi m/\beta$ ,

$$\sigma_H = \frac{\hbar^3 e^2}{A\beta} \sum_{\mathbf{k}, v_m} \frac{4\mu(\mathbf{v}_{\mathbf{k}}^* \times \mathbf{v}_{\mathbf{k}})_z \text{Tr}\{\Delta(\mathbf{k})s_z\Delta^\dagger(\mathbf{k})\}(iv_m)^2}{((i\hbar v_m)^2 - E_{1,\mathbf{k}}^2)^2((i\hbar v_m)^2 - E_{2,\mathbf{k}}^2)^2}, \quad (2.43)$$

where  $\beta$  is the inverse temperature and the sum is taken for each integer  $m$ . The numerator (2.43) in the model of Ref. 16 is given by

$$(\mathbf{v}_{\mathbf{k}}^* \times \mathbf{v}_{\mathbf{k}})_z \text{Tr}\{\Delta(\mathbf{k})s_z\Delta^\dagger(\mathbf{k})\} \quad (2.44)$$

$$= 24|\Delta|^2 \sin^2\left(\frac{\sqrt{3}}{2}k_y a\right) \left[ \cos\left(\frac{3}{2}k_y\right) - \cos\left(\frac{\sqrt{3}}{2}k_x a\right) \right]^2. \quad (2.45)$$

The expression (2.43) comes from a loop current model of d-wave superconductivity

on a honeycomb lattice, but a similar formula may apply to other multi-band chiral superconductivity models.

The Matsubara sum in (2.43) is over the following summand:

$$f(i\hbar v_m) = \frac{4(i\hbar v_m)^2}{((i\hbar v_m)^2 - E_{1,\mathbf{k}}^2)((i\hbar v_m)^2 - E_{2,\mathbf{k}}^2)}. \quad (2.46)$$

The Matsubara summation over  $f(i\hbar v_m)$  can then be replaced with a contour integral,

$$\frac{1}{\beta} \sum_{i\hbar v_m} f(i\hbar v_m) = -\frac{1}{2\pi} \int_C \frac{f(v)}{1 + \exp(\beta v)} dv, \quad (2.47)$$

in which  $C$  encloses only the imaginary axis. By deforming the contour to infinity in all directions, we find that this sum is given by residues of the integrand in Eq. (2.47) at the poles  $r$  of  $f(v)$ :

$$\frac{1}{\beta} \sum_{i\hbar v_m} f(i\hbar v_m) = \sum_r \text{Res} \left[ \frac{f(v)}{1 + \exp(\beta v)}, v = r \right] \quad (2.48)$$

$$= \left[ \frac{3E_{1,k}^2 + E_{2,k}^2}{E_{1,k}(E_{1,k}^2 - E_{2,k}^2)^3} \right] \tanh\left(\frac{\beta E_{1,k}}{2}\right) \quad (2.49)$$

$$+ \left[ \frac{3E_{2,k}^2 + E_{1,k}^2}{E_{2,k}(E_{2,k}^2 - E_{1,k}^2)^3} \right] \tanh\left(\frac{\beta E_{2,k}}{2}\right) \quad (2.50)$$

$$- \frac{\beta/2}{E_{1,k}^2 - E_{2,k}^2} \left[ \frac{1}{\cosh^2\left(\frac{\beta E_{1,k}}{2}\right)} - \frac{1}{\cosh^2\left(\frac{\beta E_{2,k}}{2}\right)} \right]. \quad (2.51)$$

In the zero-temperature limit  $\beta \rightarrow \infty$ , the Matsubara sum simplifies to

$$\frac{1}{\beta} \sum_{i\hbar v_m} f(i\hbar v_m) \rightarrow -\frac{1}{E_{1,k}E_{2,k}(E_{1,k} + E_{2,k})^3}. \quad (2.52)$$

The Hall conductivity in the zero-temperature limit is then given by formula

$$\sigma_H = \frac{e^2 \hbar^2}{\hbar A} \sum_{\mathbf{k}} \frac{\mu(\mathbf{v}_{\mathbf{k}}^* \times \mathbf{v}_{\mathbf{k}})_z \Xi_{\mathbf{k}}}{E_{1,k} E_{2,k} (E_{1,k} + E_{2,k})^3} = -\frac{e^2 \mu}{\hbar t} \left( \frac{|\Delta|}{t} \right)^2 F \quad (2.53)$$

$$F = 48\pi t^5 \int_{BZ} d^2k \frac{\sin^2(\frac{\sqrt{3}}{2}k_y) \left( \cos(\frac{3}{2}k_y) - \cos(\frac{\sqrt{3}}{2}k_x) \right)^2}{E_{1,k} E_{2,k} (E_{1,k} + E_{2,k})^3}. \quad (2.54)$$

We estimate  $\sigma_H$  by combining equations (2.39), (2.40), and (2.42) to obtain

$$\sigma_H \approx \frac{e^2 \mu}{\hbar t} \left( \frac{|\Delta|}{t} \right)^2 \ln\left(\frac{t}{\Delta}\right) \frac{1}{d} = 4 \times 10^{13} \text{ Hz} = 40 \text{ THz (CGS ESU)} \quad (2.55)$$

$$= 4000 \text{ S/m (SI)}. \quad (2.56)$$

Here we assume the chemical potential to be  $\mu \approx 0.5t$ , the superconducting gap to be  $\Delta \approx 0.1t$ , and the interlayer spacing in the z-direction to be  $d \approx 1 \times 10^{-8}$  cm. Our estimate for the Hall conductivity satisfies our prior assumption (2.38).

## 2.6 Experimental Proposal

We propose a simple measurement of the Hall voltage  $V_r^H$  across a superconducting sample with Corbino geometry. In our analysis we considered the limit of an infinitely long cylinder, because it is simpler in theory, but in an experiment a thin washer geometry is more practical. In Fig. 2.2 we depict an annular sample with intermediate thickness brought into proximity with a coaxial cable by a conical metallic waveguide and subjected to an oscillating magnetic field along the z-axis. As discussed in section 2.4 this oscillating magnetic field should give rise to charge

oscillations and a potential difference  $V_r^H$  across the sample.

The sample does not touch the waveguide due to insulating material indicated by thick black lines in Fig. 2.2, but the potential difference  $V_r^H$  is induced between the inside and outside of the coaxial cable when charge oscillations are present. This contactless measurement avoids difficulties in establishing an Ohmic contact for current-based voltage measurement.

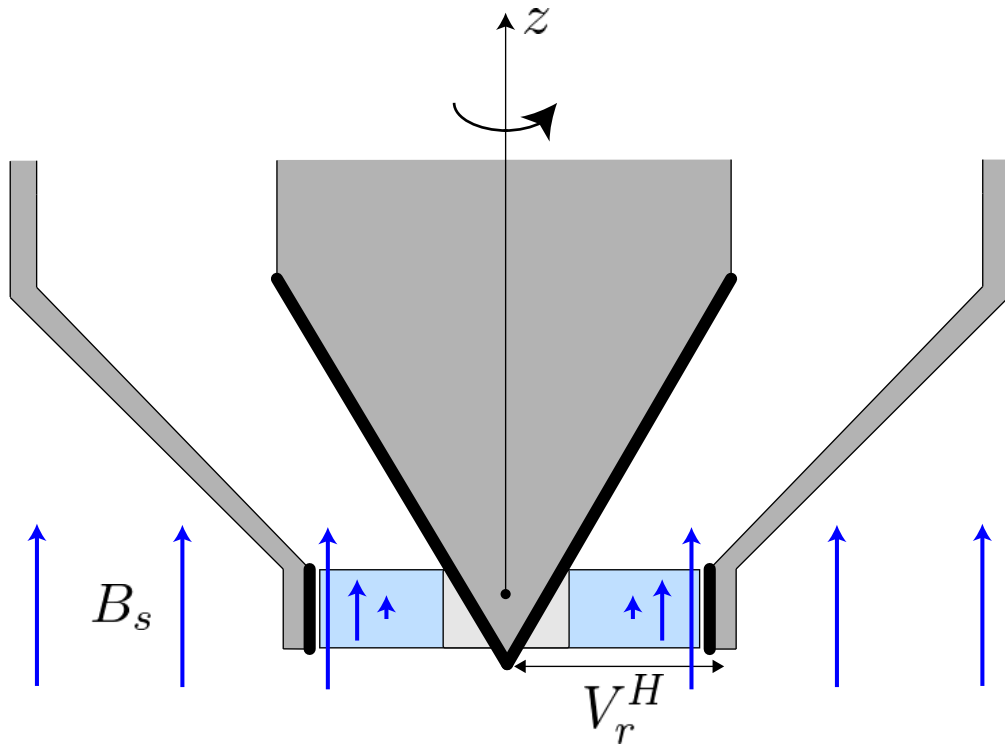


Figure 2.2: Our proposed experimental setup uses a waveguide nozzle at the end of a coaxial cable to measure the potential difference  $V_r^H$ . The thick black lines represent insulating coating on the inside of the waveguide, so that the voltage measurement is contactless. The applied magnetic field  $\mathbf{B}_0$  of the external solenoid is represented by purple arrows.

There have been many Hall effect measurements for normal metals and semiconductors using microwave cavities and microwave resonators [32–35]. However, the superconducting case is complicated by the presence of Meissner screening, and



it would take some additional work to see how those methods may be adopted to the superconducting case.

An estimate for the Hall voltage (2.36) depends on the material's London frequency, which we estimate to be  $\omega_L = c/100\text{nm} = 3000 \text{ THz}$ , and its Hall frequency, which we take from (2.56) to be  $\sigma_H = 40 \text{ THz}$ .

As for the applied magnetic field, in our calculation we assumed the magnetic field was low enough to avoid the creation of vortices ( $B_0 < H_{c1}$ ) for theoretical simplicity, but in experiment the only real limit is the upper critical field ( $B_0 < H_{c2}$ ). We also assumed the frequency of the solenoid creating the field is low enough to avoid electromagnetic retardation in our calculation, but this is also not binding on experiment. For our calculation, we assume the magnetic field of the relatively low magnitude  $B_0 = 100 \text{ mT}$  that is driven at a linear frequency  $f = \omega/2\pi = 100 \text{ GHz}$ .

Using the numbers we have given, we find the magnitude of the Hall voltage in (2.36), in SI units, to be the following:

$$V_r^H = 7 \text{ nV} \left( \frac{f}{100\text{GHz}} \right)^2 \left( \frac{B_0}{100\text{mT}} \right) \left( \frac{\lambda_L}{100\text{nm}} \right)^4. \quad (2.57)$$

The power at the end of the coaxial cable with resistance  $R = 50\Omega$  would then be given by  $P = (V_r^H)^2/R \approx 10^{-18} \text{ W}$ . The surface charge density in (2.35), in SI units, is then

$$q = 2 \times 10^{-16} \text{ C/cm}^2. \quad (2.58)$$

It should also be noted that a trade-off exists between exploring the anomalous Hall conductivity at lower frequencies and obtaining a large enough Hall voltage to make the experiment practical.

Our analysis considered an infinite cylinder for simplicity, however in practice the sample would be of finite. The experimentally relevant geometry is a Corbino disk with a small thickness, but this situation is more complicated. For a thin-film in the shape of a Corbino disk, the London penetration depth would be superseded by the longer Pearl distance  $\lambda_L^2/L$  [36], where  $L$  is thickness, but since the thin-film does not perfectly shield the bulk the situation is different and would need a separate analysis in some future work. The thin-film should also have strongly enhanced magnetic flux at its edges making the nucleation of vortices more likely.

## 2.7 Induced Hall Conductivity

So far we have assumed that the Hall conductivity is intrinsic to the superfluid and not induced by the applied axial magnetic field. In the previous sections we found that a spontaneous Hall conductivity leads to a charge and voltage response linear in the applied axial magnetic field  $B_s(t)$ . However, the applied magnetic field inside the London penetration depth can produce an extrinsic non-linear Hall effect, which we can compare with the linear Hall effect caused by intrinsic Hall conductivity. Hall conductivity of extrinsic origin depends on the magnetic field,

$$\sigma_H^E(r, t) = s_H B_z(r, t), \quad (2.59)$$

and therefore have the time dependence of the applied axial magnetic field. The circular electric field and axial magnetic fields in Eq. (2.21) and Eq. (2.20) have the time-dependence

$$B_z(r, t) = B_z(r) \cos(\omega t) \quad (2.60)$$

$$E_\theta(r, t) = -\frac{\lambda_L}{c} B_z(r) \sin(\omega t) \quad (2.61)$$

where  $B_z(r)$  gives the radial dependence of the magnetic field in the superconductor.

If we replace  $\sigma_H \rightarrow \sigma_H^E(r, t)$  then the radial Hall current from Eq. (2.7) is given by

$$j_r^H(r, t) = -s_H B_z(r) \cos(\omega t) \frac{\lambda_L}{c} B_z(r) \sin(\omega t) \quad (2.62)$$

$$= -\frac{s_H \lambda_L}{2c} B_z^2(r) \sin(2\omega t). \quad (2.63)$$

Hall conductivity induced by the external magnetic field responds non-linearly at the frequency  $2\omega$ . This second harmonic response is also seen in the surface charge density and Hall voltage. Rederiving the Hall voltage and surface charge density using Eq. (2.29) and Eq. (2.30) in the time domain (with  $\sigma_H \rightarrow \sigma_H^E(r, t)$ ) we find

$$q(t) \approx -\frac{\omega^2 s_H}{2\omega_L^3} B_z^2(R_o) \cos(2\omega t) \quad (2.64)$$

and

$$V_H \approx -\frac{2\pi s_H \omega^2 c}{\omega_L^4} B_z^2(R_o) \cos(2\omega t). \quad (2.65)$$

Both a conventional and TRSB superconductor may have non-linear  $2\omega$  charge oscillations caused by the applied magnetic field, but only a TRSB superconductor with a spontaneous Hall conductivity has a linear response at the driving frequency.

## 2.8 Charge Oscillation in General

So far we have investigated charge oscillation in a specific geometry. Now let us consider this phenomenon more generally. We will begin by deriving a differential equation for the dynamics of charge in the bulk. For completeness we will include a possible normal current  $\mathbf{j}^N = \sigma_N \mathbf{E}$ .

### 2.8.1 Local Oscillation in Charge Density

Consider Ampere's Law in the case of normal, Hall, and super- currents,

$$\nabla \times \mathbf{B} = \frac{4\pi}{c} (\mathbf{j}^S + \mathbf{j}^N + \mathbf{j}^H) + \frac{1}{c} \frac{\partial \mathbf{E}}{\partial t}. \quad (2.66)$$

Taking the divergence of Ampere's Law gives the charge continuity equation,

$$\frac{\partial \rho}{\partial t} = -\nabla \cdot (\mathbf{j}^S + \mathbf{j}^N + \mathbf{j}^H). \quad (2.67)$$

Writing the normal and Hall currents in terms of the electric field, equation (2.67)

becomes

$$\frac{\partial \rho}{\partial t} = -\nabla \cdot \mathbf{j}^S - \sigma_N \nabla \cdot \mathbf{E} - \sigma_H (\nabla \times \mathbf{E})_z. \quad (2.68)$$

Using Gauss' Law and Faraday's Law, our expression becomes

$$\frac{\partial \rho}{\partial t} = -\nabla \cdot \mathbf{j}^S - 4\pi\sigma_N \rho - \frac{\sigma_H}{c} \frac{\partial B_z}{\partial t}. \quad (2.69)$$

Finally, by taking the time-derivative of both sides of our equation and using the first London relation (2.5), we obtain a differential equation relating the local charge  $\rho$  to the local magnetic field  $B_z$ :

$$\frac{\partial^2 \rho}{\partial t^2} = -\omega_L^2 \rho - 2\omega_N \frac{\partial \rho}{\partial t} - \frac{\sigma_H}{c} \frac{\partial^2 B_z}{\partial t^2}, \quad (2.70)$$

where we define  $\omega_N = 2\pi\sigma_N$ .

We can first solve the homogenous part of equation (2.70) in the case where there is no applied magnetic field,

$$\frac{\partial^2 \rho}{\partial t^2} = -\omega_L^2 \rho - 2\omega_N \frac{\partial \rho}{\partial t}. \quad (2.71)$$

If we substitute  $\rho = P e^{-\omega_N t}$  in (2.71), we obtain the simpler equation

$$\frac{\partial^2 P}{\partial t^2} = -(\omega_L^2 - \omega_N^2) P. \quad (2.72)$$

This second-order differential equation describes simple harmonic motion at the frequency  $\sqrt{\omega_L^2 - \omega_N^2}$ . The solution for  $\rho$  can then be found easily:

$$\rho(\mathbf{r}, t) = \rho(\mathbf{r}) \cos\left(t\sqrt{\omega_L^2 - \omega_N^2}\right) e^{-\omega_N t}. \quad (2.73)$$

The initial charge distribution  $\rho(\mathbf{r}, 0)$  maintains its shape in space with each point acting as a damped oscillator. At zero temperature,  $\sigma_N = 0$  and the charge should oscillate at the plasma frequency forever, but until now no one has claimed to observe these plasma oscillations in the superconductor. However, without the inhomogeneous term coming from Hall conductivity, there is no source for these oscillations.

Now let us solve the inhomogeneous case of equation (2.70) for a magnetic field  $B_z(\mathbf{r}, t) = B_z(\mathbf{r})e^{i\omega_0 t}$ . Once again we make the substitution  $\rho = Pe^{-\omega_N t}$  to obtain a simplified equation,

$$\frac{\partial^2 P}{\partial t^2} = -\left(\omega_L^2 - (2\pi\sigma_N)^2\right)P - \frac{\sigma_H}{c} e^{2\pi\sigma_N t} \frac{\partial^2 B_z(\mathbf{r}, t)}{\partial t^2}. \quad (2.74)$$

We can then solve it in the frequency domain,

$$P(\mathbf{r}, \omega) = \frac{\sigma_H}{c} \frac{\omega_0^2}{\omega_L^2 - \omega_N^2 - \omega^2} B_z(\mathbf{r}) \delta(\omega - \omega_0 + i\omega_N). \quad (2.75)$$

Finally, we find the bulk charge density in the time domain,

$$\rho(\mathbf{r}, t) = \frac{\sigma_H}{c} \frac{\omega_0^2}{\omega_L^2 - \omega_0^2 + 2i\omega_N\omega_0} B_z(\mathbf{r}) e^{i\omega_0 t}. \quad (2.76)$$

Thus, we see the Hall effect leads to oscillations in the local charge density  $\rho(r, t)$ , while in the absence of the Hall effect the oscillating charge is exponentially damped by normal current. From this perspective it makes sense that experimenters have not seen plasma oscillations in the superconductor.

## 2.8.2 Oscillation in Total Surface Charge

An alternative way to view the oscillation of charge in a superconductor can be understood by considering a simply connected superconducting sample occupying the volume  $V$  and having net zero charge. In this case we will derive a damped harmonic oscillator involving the total charge on the boundary  $\partial V$ ,

$$Q(t) = - \int_V \rho(\mathbf{r}, t) d^3 \mathbf{r}, \quad (2.77)$$

defined as opposite the charge in the total volume of the bulk.

We can obtain a charge continuity equation for  $Q(t)$  by integrating the continuity equation (2.67):

$$\frac{\partial Q}{\partial t} = \int_V \nabla \cdot (\mathbf{j}^S + \mathbf{j}^H + \mathbf{j}^N) d^3 \mathbf{r}. \quad (2.78)$$

Then, using the Gauss's Law and the definition  $\mathbf{j}^N = \sigma_N \mathbf{E}$ , we write

$$\frac{\partial Q}{\partial t} = \int_{\partial V} (\mathbf{j}^S + \mathbf{j}^H + \sigma_N \mathbf{E}) \cdot d\mathbf{A} = I^S + I^H - 2\omega_N Q(t). \quad (2.79)$$

Here  $I^S$  and  $I^H$  are the total supercurrent and Hall current at the boundary  $\partial V$ , respectively. The Hall current at the boundary can be related to the total flux through the superconducting sample in the following way:

$$I^H = \int_{\partial V} \mathbf{j}^H \cdot d\mathbf{A} = \sigma_H \int_V \nabla \cdot (\mathbf{E} \times \hat{\mathbf{z}}) d^3\mathbf{r} = \frac{\sigma_H}{c} \frac{\partial}{\partial t} \int_V B_z(\mathbf{r}) d^3\mathbf{r}. \quad (2.80)$$

Next, we obtain an equation of motion for  $Q(t)$  by integrating the first London equation (2.5) over  $\partial V$  to obtain

$$\frac{\partial I^S}{\partial t} = \frac{n_s e^2}{m} \int_{\partial V} \mathbf{E} \cdot d\mathbf{A} = -\frac{4\pi n_s e^2}{m} Q = -\omega_L^2 Q. \quad (2.81)$$

Combining our two equations, we have a damped harmonic oscillator driven by the total magnetic field penetrating the superconductor:

$$\frac{\partial I^S}{\partial t} = -\omega^2 Q(t), \quad (2.82)$$

$$\frac{\partial Q}{\partial t} + 2\omega_N Q(t) = I^S + I^H, \quad (2.83)$$

$$I^H = \frac{\sigma_H}{c} \frac{\partial}{\partial t} \int_V B_z(\mathbf{r}) d^3\mathbf{r}. \quad (2.84)$$

These oscillator equations apply to any TRSB superconductor placed in a time-varying magnetic field or moving in a non-uniform magnetic field.



## 2.9 Solenoid Threading the Superconductor

In this section, we consider the alternative of placing the solenoid inside the annular cylinder of inner radius  $R_i$  and outer radius  $R_o$ , and find that the results are the same as placing the solenoid outside of the superconductor, except that the screening of the electromagnetic field is more complicated. This approach has the downside of the solenoid being smaller, which limits the possible current and field through the solenoid. The smaller solenoid has the advantage that it has less inductance and can be driven at a higher frequency. Consequently, we work in terms of an ac linear current density  $I_\omega^{2D}$  (measured in biots/cm) of the solenoid, which occurs at the radius  $R_s$  inside the circular cavity of radius  $R_i$ .

Since the superconductor shields electrodynamic activity from its bulk, nothing interesting happens far away from the interface at  $r = R_i$ , and for our purposes the outer edge of the cylinder can be taken to be infinity. We treat the solenoid-superconductor system perturbatively in  $\sigma_H$  by first finding the electromagnetic behavior for a normal superconductor ( $\sigma_H = 0$ ) and then showing that charge oscillation occurs as a first-order effect in  $\sigma_H \neq 0$ . Throughout this section we work in the Fourier domain.

The electromagnetic field in the cavity is determined both by the driving linear current density  $I_\omega^{2D}$  of the solenoid and the supercurrent response current density  $I_{sc}^{2D}$  of the superconductor. Since the solenoid current creates a time-dependent magnetic flux, we know from Lenz's law that there should be a current in the superconductor to create an opposing magnetic flux. The electric field in vacuum ( $R_s < r < R_i$ )

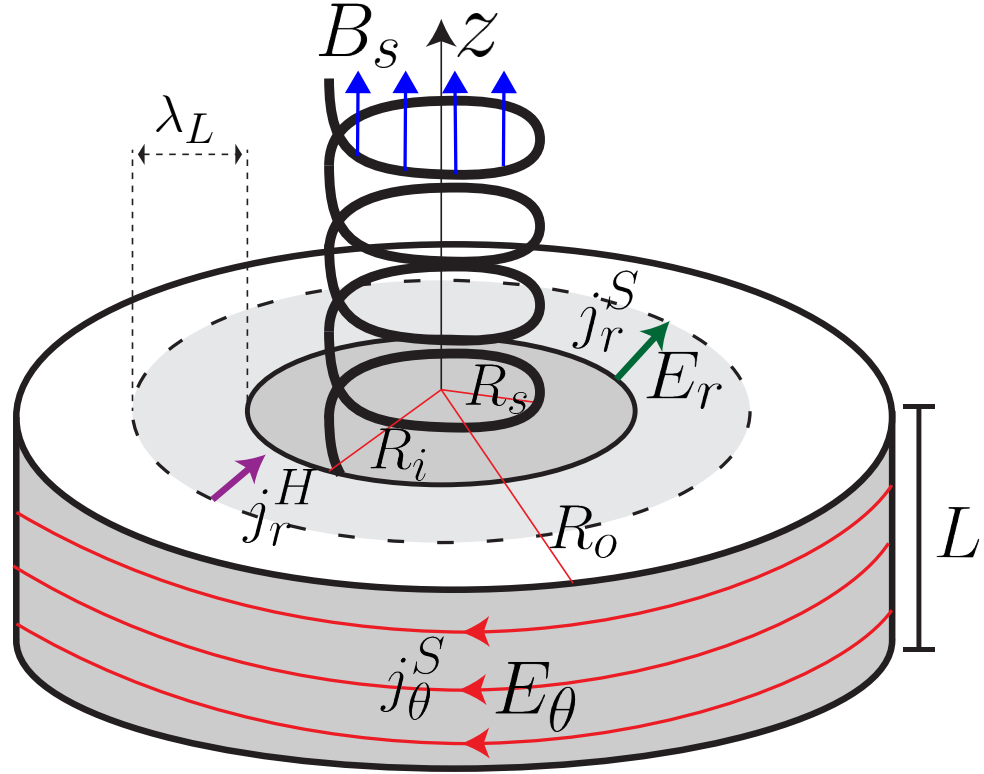


Figure 2.3: A solenoid of radius  $R_s$  threading an superconducting annular cylinder of inner radius  $R_i$ , outer radius  $R_o$ , and length  $L$ . The axial magnetic field  $\mathbf{B}_s$  of the solenoid induces radial Hall current  $j_r^H$  which is compensated by radial supercurrent  $j_r^S$  within a London penetration depth  $\lambda_L$  of the inner surface of the superconductor. Since the effects happen near the inner surface of the superconductor, the outer radius  $R_o$  can be taken to be infinite.

and in the superconductor ( $r > R_i$ ) depend on each other, and we must use the condition that the electric and magnetic fields be continuous at  $r = R_i$  to find a solution which is self-consistent.

### 2.9.1 Field in “Vacuum” $R_s < r < R_i$

In the region  $R_s < r < R_i$  there is vacuum between the solenoid at  $r = R_s$  and the edge of the superconductor at  $r = R_i$ . We assume the quasi-static limit,

$$\omega \ll \frac{c}{R_i} \quad (2.85)$$

in which retardation can be neglected. In this low-frequency limit [37], it is known that an ideal solenoid with ac current density  $I_\omega^{2D}$  contains a time-dependent magnetic field  $B'_z(r < a) = 4\pi I_\omega^{2D}/c$  completely contained within its coils, and produces a circularly oriented electric field  $E_\theta(r)$  at  $r > R_s$ . By Faraday’s Law (2.2), we determine the electric field  $\mathbf{E}'$  produced by the solenoid:

$$\int_{|s|=r} \mathbf{E}' \cdot d\mathbf{s} = -\frac{1}{c} \frac{d}{dt} \int \mathbf{B}' \cdot d\mathbf{A}, \quad (2.86)$$

$$B'_z(R_s < r < R_i) = 0, \quad (2.87)$$

$$E'_\theta(R_s < r < R_i) = \frac{i2\pi\omega R_s^2}{c^2 r} I_\omega^{2D}, \quad (2.88)$$

where we have integrated over a circular contour of radius  $r$ .

However, since this circularly oriented electric field can also excite a circular current density  $I_{sc}^{2D}$  on the inner surface of the superconductor, we expect an additional constant contribution to the magnetic field  $B''_z(r < R_i) = 4\pi I_{sc}^{2D}/c$  and a corresponding contribution to the electric field  $E''_\theta$  determined by Faraday’s Law

(2.2),

$$\int_{|s|=r} \mathbf{E}' \cdot d\mathbf{s} = -\frac{1}{c} \frac{d}{dt} \int \mathbf{B}'' \cdot d\mathbf{A}, \quad (2.89)$$

$$B_z''(R_s < r < R_i) = \frac{4\pi}{c} I_{sc}^{2D}, \quad (2.90)$$

$$E_\theta''(R_s < r < R_i) = \frac{i\omega r}{2c} B_z'' = \frac{i2\pi\omega r}{c^2} I_{sc}^{2D}. \quad (2.91)$$

The total electromagnetic field inside the cavity ( $R_s < r < R_i$ ) is then

$$E_\theta(r) = E_\theta'(r) + E_\theta''(r) = \frac{i2\pi\omega R_i^2}{c^2 r} I_\omega^{2D} + \frac{i\omega r}{2c} B_z'', \quad (2.92)$$

$$B_z(r) = B_z'(r) + B_z''(r) = B_z''. \quad (2.93)$$

Because the electric and magnetic field must be continuous at the interface between vacuum and the superconductor at  $r = R_i$ , we use Eq. (2.91) as a boundary condition to find the electromagnetic field in the superconductor at  $r > R_i$ . We then find an expression for  $B_z''$  in terms of the driving current density  $I_\omega^{2D}$ .

### 2.9.2 Screening in the Superconductor $r > R_i$

Now we solve for the screened electromagnetic field within the superconducting cylinder. In contrast to the case of the outer solenoid, in this section we do not treat the Hall effect as a perturbation. In the Fourier domain, Faraday's Law, Eq. (2.2), is given by

$$\nabla \times \mathbf{E} = \frac{i\omega}{c} \mathbf{B}. \quad (2.94)$$

Similarly, for Ampere's Law, Eq. (2.3), we replace  $\mathbf{j}^S$  using the London relation, Eq. (2.5), and  $\mathbf{j}^H$  using Eq. (2.7). This gives us

$$\nabla \times \mathbf{B} = \frac{4\pi\sigma_H}{c} \mathbf{E} \times \hat{\mathbf{z}} - \frac{i\omega}{c} \left[ 1 - \frac{\omega_L^2}{\omega^2} \right] \mathbf{E}. \quad (2.95)$$

Since we are assuming that the system is infinitely long and cylindrically symmetric, the  $\theta$  and  $z$  derivatives vanish in equations (2.94) and (2.95). The vanishing of these derivatives leads to the r-component of the curl being zero, as seen in the discussion preceding equation (2.28). Consequently, the r-component equation of (2.95) gives a relationship between  $E_r$  and  $E_\theta$ :

$$\frac{i\omega}{c} E_r = \frac{4\pi}{c} (j_r^S + j_r^H) = \frac{\omega_L^2}{c\omega} E_r + \frac{4\pi\sigma_H}{c} E_\theta, \quad (2.96)$$

which we solve to find

$$E_r(r, \omega) = i \frac{4\pi\sigma_H \omega c^2}{(\omega_L^2 - \omega^2)^{3/2}} E_\theta(r, \omega). \quad (2.97)$$

As a result, we can eliminate  $E_r$  together with the  $\theta$  and  $z$  derivatives from the Maxwell equations (2.94) and (2.95) to obtain  $B_r = 0$ , and the following two uncoupled sets of equations:

$$\frac{\partial E_\theta}{\partial r} + \frac{E_\theta}{r} = \frac{i\omega}{c} B_z \quad (2.98)$$

$$\frac{\partial B_z}{\partial r} = -\frac{ic}{\omega} \left[ \frac{\omega_L^2 - \omega^2}{c^2} - \frac{4\pi\sigma_H^2}{c^2} \frac{\omega^2}{\omega_L^2 - \omega^2} \right] E_\theta, \quad (2.99)$$

and

$$\frac{\partial E_z}{\partial r} = \frac{i\omega}{c} B_\theta \quad (2.100)$$

$$\frac{\partial B_\theta}{\partial r} + \frac{B_\theta}{r} = -\frac{ic\omega_L^2 - \omega^2}{\omega c^2} E_z. \quad (2.101)$$

These equations differ from (2.15) and (2.16) by a modification to the dielectric function. Since only  $E_\theta \neq 0$  at the boundary, we can also assume  $E_z = B_\theta = 0$  and focus on the equations for  $E_\theta$  and  $B_z$ . Combining Eq. (2.98) and Eq. (2.99), we obtain modified Bessel differential equations,

$$\frac{\partial^2 E_\theta}{\partial r^2} + \frac{1}{r} \frac{\partial E_\theta}{\partial r} - \frac{1}{r^2} E_\theta = \kappa^2(\omega) E_\theta \quad (2.102)$$

$$\frac{\partial^2 B_z}{\partial r^2} + \frac{1}{r} \frac{\partial B_z}{\partial r} = \kappa^2(\omega) B_z, \quad (2.103)$$

of order one and zero respectively. Here

$$\kappa^2(\omega) = \frac{1}{\lambda^2(\omega)} \frac{\omega_L^2 - \omega^2}{c^2} - \frac{4\pi\sigma_H^2}{c^2} \frac{\omega^2}{\omega_L^2 - \omega^2}. \quad (2.104)$$

The modified Bessel equation of order  $n$  has an exponentially decaying solution  $K_n$  and an exponentially growing solution  $I_n$ , which we discard. The Bessel Equation (2.17) gives us an electric field inside the superconductor,

$$E_\theta(r) = C_s K_1(\kappa(\omega)r). \quad (2.105)$$

If we substitute our expression for  $E_\theta(r)$  in Eq. (2.105) into Eq. (2.98), we obtain a

magnetic field that solves Eq. (2.99):

$$B_z(r) = i \frac{c\kappa(\omega)}{\omega} C_s K_0(\kappa(\omega)r). \quad (2.106)$$

Using the continuity of  $E_\theta(r)$  and  $B_z(r)$  at the interface, we can find  $C_s$  for  $r > R_i$  and  $B_z''$  for  $r < R_i$  by setting the expressions in Eq. (2.92) and Eq. (2.93) equal to the expressions in Eq. (2.105) and Eq. (2.106) with  $r = R_i$ . We find

$$C_s = i \frac{4\pi\omega R_s^2}{2R_i c^2 K_1(\kappa R_i) + \kappa R_i^2 c^2 K_0(\kappa R_i)} I_\omega^{2D}, \quad (2.107)$$

$$B_z'' = - \frac{4\pi\kappa a^2 K_0(\kappa b)}{2R_i c K_1(\kappa R_i) + \kappa R_i^2 c K_0(\kappa R_i)} I_\omega^{2D}. \quad (2.108)$$

If, for a consistency check, we set  $\omega_L \rightarrow 0$  and  $\sigma_H \rightarrow 0$  in Eq. (2.104), i.e., there is no superconductor, we can show that our electromagnetic field becomes the solution for a solenoid in vacuum. Then, in the limit  $\omega_L \rightarrow 0$ ,  $\kappa \rightarrow i\omega/c$ . Since  $\omega \ll c/R_i$  (from Eq. (2.85)), we can then use the small argument expansions of the Bessel functions,  $K_0(\kappa r) \approx -\ln(\omega r/c)$  and  $K_1(\kappa r) \approx c/(i\omega r)$ , where  $-\ln(\omega r/c) \ll c/(i\omega r)$ , to reduce (2.105) and Eq. (2.106) to the field of a solenoid in vacuum given in Eq. (2.88) and Eq. (2.87).

For our case we make the low-frequency assumption,

$$\omega \ll \omega_L, \quad (2.109)$$

in which case the screening length

$$\lambda(\omega) = \frac{1}{\kappa(\omega)} \quad (2.110)$$

is approximately the London length,  $\lambda(\omega \ll \omega_L) = \lambda_L$ . Assuming  $c/R_i < \omega_L$ , the low-frequency limit in Eq. (2.109) is less restrictive than the low-frequency limit we assumed to avoid electromagnetic retardation in Eq. (2.85), so it follows naturally. In this limit, since  $r > R_i \gg \lambda_L$  we can use the large argument Bessel function approximations,  $K_n(z) \approx \sqrt{\pi/2z}e^{-z}$ , with  $z = r/\lambda(\omega) \gg 1$ , in Eq. (2.105) and Eq. (2.106),

$$E_\theta(r) \approx i \frac{4\pi R_s^2}{cR_i^2} \frac{\omega}{\omega_L} I_\omega^{2D} \sqrt{\frac{R_i}{r}} e^{-(r-R_i)/\lambda(\omega)} \quad (2.111)$$

$$B_z(r) \approx -\frac{4\pi R_s^2}{cR_i^2} I_\omega^{2D} \sqrt{\frac{R_i}{r}} e^{-(r-R_i)/\lambda(\omega)}. \quad (2.112)$$

The Eqns. (2.111) and (2.112) are the electrical analog of the usual Meissner effect in which a static magnetic field is shielded from the bulk of a superconductor.

The electric field, which was initially caused by the changing flux of the solenoid, creates a circular supercurrent,

$$j_\theta^S = i \frac{\omega_L^2}{4\pi\omega} E_\theta \approx -\frac{R_s^2}{R_i^2} \frac{\omega_L}{c} I_\omega^{2D} \sqrt{\frac{R_i}{r}} e^{-(r-R_i)/\lambda(\omega)}. \quad (2.113)$$

The supercurrent  $j_\theta^S$  flows near the inner surface of the superconductor and forms a solenoidal linear current density  $I_{sc}^{2D}$  of radius  $r = R_i$  coaxial to the physical solenoid



at  $r = R_s$ . We calculate  $I_{sc}^{2D}$  and see that it gives rise to a flux  $\Phi_{sc}$  in the cavity ( $r < R_i$ ) exactly opposite to that of the solenoid flux  $\Phi_{sol}$ :

$$I_{sc}^{2D} = \int_b^\infty j_\theta^S dr \approx -\frac{R_s^2}{R_i^2} I_\omega^{2D} \quad (2.114)$$

$$B_z'' = \frac{4\pi}{c} I_{sc}^{2D} \approx -\frac{4\pi}{c} \frac{R_s^2}{R_i^2} I_\omega^{2D} \quad (2.115)$$

$$\Phi_{sc} = \pi R_i^2 B_z'' \approx -\pi R_s^2 \frac{4\pi}{c} I_\omega^{2D} = -\Phi_{sol}. \quad (2.116)$$

The zero-net-flux condition

$$\Phi_{sc} + \Phi_{sol} = 0 \quad (2.117)$$

is an expression of Lenz's Law in the case where there are no vortices in the superconductor, consistent with our discussion below Eq. (2.4). The supercurrent density  $I_{sc}^{2D}$  is always proportional to  $I_\omega^{2D}$  because the superconductor opposes any net change to the total flux. These two solenoidal currents are even proportional in the dc limit  $\omega \rightarrow 0$  because their changes must always be coordinated to keep the total flux constant. Since the total flux through the superconductor cannot change, the electric field is shielded from the bulk of the superconductor.

In this section we considered a solenoid threading the inside of the superconductor, rather than being outside of the superconductor. In this case we did not treat  $\sigma_H$  perturbatively, to show that the only effect is a renormalization of the inverse penetration depth  $\kappa$  in (2.104) by the addition of a negligible factor proportional to  $\sigma_H^2$ . This factor is negligible so long as  $\sigma_H \ll \omega_L^2/\omega$ , as in equation (2.38).

The Hall conductivity has only a tiny impact on the circular electric field or on the axial magnetic field in the material. In the next section we consider the radial Hall effect and charge oscillation induced by the circular electric field.

### 2.9.3 Radial Charge Oscillation

If the superconductor at  $r > R_i$  breaks time-reversal symmetry, then a small anomalous Hall conductivity  $\sigma_H$  is possible. The immediate consequence is a Hall current density  $\mathbf{j}^H \neq 0$  from Eq. (2.7) that allows for a radial electric field  $E_r \neq 0$ . The radial Hall current is given by:

$$j_r^H(r) = \sigma_H E_\theta(r). \quad (2.118)$$

Using the approximation of  $E_\theta(r)$  in Eq. (2.111), we see the radial Hall current decays into the bulk,

$$j_r^H(r) \approx i \frac{\sigma_H}{c} \frac{4\pi R_s^2}{R_i^2} \frac{\omega}{\omega_L} I_\omega^{2D} \sqrt{\frac{R_i}{r}} e^{-(r-R_i)/\lambda(\omega)}. \quad (2.119)$$

We also saw that the radial electric field  $E_r$  in equation (2.97) is given in terms of  $E_\theta$ , which is given by Eq. (2.111). Thus, the radial electric field also exponentially decays into the bulk,

$$E_r(r) \approx \frac{4\pi\sigma_H}{\omega_L^2 - \omega^2} \frac{4\pi R_s^2}{R_i^2} \frac{\omega^2}{c\omega_L} I_\omega^{2D} \sqrt{\frac{R_i}{r}} e^{-(r-R_i)/\lambda(\omega)}. \quad (2.120)$$

The radial electric field has several implications: a surface charge on the inner boundary of the superconductor, a Hall voltage between the inner and outer boundaries of the superconductor, and a radial supercurrent.

The jump in the radial component in the electric field from  $E_r(r < R_i) = 0$  in the cavity to  $E_r(r > R_i) \neq 0$  in the superconductor corresponds to a surface charge  $Q_{R_i}$  within a Thomas-Fermi screening length of the surface at  $r \approx R_i$ . Because the Thomas-Fermi length is small compared to the length scale  $\lambda(\omega)$ , we treat the charge as residing on the cylindrical surface of area  $A = 2\pi R_i L$ . From Gauss' Law and Eq. (2.120), we conclude

$$Q_{R_i} = \frac{A}{4\pi} E_r(R_i) \approx \frac{2\pi R_i L \sigma_H}{\omega_L^2 - \omega^2} \frac{4\pi R_s^2}{R_i^2} \frac{\omega^2}{c\omega_L} I_\omega^{2D}. \quad (2.121)$$

The radial electric field in Eq. (2.97) can also be integrated to give us the Hall voltage  $V_H$  between the inside and outside of the cylinder associated with the built-up charge  $Q_{R_i}$ :

$$V_r^H = - \int_b^\infty E_r dr = -i \frac{4\pi\omega\sigma_H}{\omega_L^2 - \omega^2} \int_b^\infty E_\theta dr. \quad (2.122)$$

Using Eq. (2.99) to substitute for  $E_\theta$ , we find

$$V_r^H = -i \frac{4\pi\omega\sigma_H}{\omega_L^2 - \omega^2} \frac{i\omega}{c\kappa^2} \int_b^\infty \frac{\partial B_z(r)}{\partial r} dr = - \frac{4\pi c\sigma_H}{\omega_L^2 - \omega^2} \frac{\omega^2}{c\kappa^2} B_z(b). \quad (2.123)$$

Using Eq. (2.112) to approximate the Hall voltage in Eq. (2.123) in terms of  $I_\omega^{2D}$  we

obtain,

$$V_H \approx \frac{4\pi\sigma_H}{\omega_L^2 - \omega^2} \frac{\omega^2}{\omega_L^2} \frac{4\pi R_s^2}{R_i^2} I_\omega^{2D}. \quad (2.124)$$

The Hall resistance of the superconducting cylinder can then be defined as

$$R_H = \frac{V_H}{d_{\text{coil}} I_\omega^{2D}} = \frac{4\pi\sigma_H}{\omega_L^2 - \omega^2} \frac{\omega^2}{\omega_L^2} \frac{4\pi R_s^2}{d_{\text{coil}} R_i^2}, \quad (2.125)$$

where  $d_{\text{coil}}$  is the distance between coils in the solenoid.

The radial electric field also causes supercurrent to contribute to the total radial current. We find the radial supercurrent by substituting our expression for  $E_r$  from from Eq. (2.97) into Eq. (2.5):

$$j_r^S(r) = i \frac{\omega_L^2}{4\pi\omega} E_r(r) = -\frac{\sigma_H \omega_L^2}{\omega_L^2 - \omega^2} E_\theta(r). \quad (2.126)$$

The combined supercurrent and Hall current in the radial direction is

$$j_r(r) = j_r^S(r) + j_r^H(r) = -\frac{\sigma_H \omega^2}{\omega_L^2 - \omega^2} E_\theta(r). \quad (2.127)$$

In terms of our approximation for  $E_\theta$  from Eq. (2.111), our expression Eq. (2.127) gives

$$j_r(r) \approx i \frac{4\pi\sigma_H \omega^2}{\omega_L^2 - \omega^2} \frac{\omega}{\omega_L} \frac{R_s^2}{c R_i^2} I_\omega^{2D} \sqrt{\frac{R_i}{r}} e^{-(r-R_i)/\lambda(\omega)}. \quad (2.128)$$

The total current is proportional to the small factor  $\omega^2/\omega_L^2$ , since the supercurrent partially cancels the effect of the Hall current. Since both the supercurrent and Hall currents decay into the bulk with the electromagnetic field, the charge  $Q_{R_i}$  that accumulates at the boundary must be compensated by a charge distribution  $\rho$  within the London penetration depth of the superconductor. We solve for  $\rho(r)$  using Eq. (2.70) (with  $\sigma_N = 0$ ) in the Fourier domain:

$$\rho(r) = -\frac{\sigma_H}{c} \frac{\omega^2}{\omega_L^2 - \omega^2} B_z(r). \quad (2.129)$$

Using Eq. (2.112) in Eq. (2.129) gives us a charge distribution which also decays into the bulk,

$$\rho(r) \approx \frac{4\pi\sigma_H\omega^2}{\omega_L^2 - \omega^2} \frac{R_s^2}{c^2 R_i^2} I_\omega^{2D} \sqrt{\frac{R_i}{r}} e^{-(r-R_i)/\lambda_L}. \quad (2.130)$$

We can compare the bulk charge density with the surface charge density by integrating  $\rho$  in Eq. (2.129) over the volume of the superconductor:

$$Q = 2\pi L \int_{R_i}^{\infty} dr r \rho(r) \quad (2.131)$$

$$= -\frac{2\pi L \sigma_H}{c} \frac{\omega^2}{\omega_L^2 - \omega^2} \int_{R_i}^{\infty} r B_z(r) dr. \quad (2.132)$$

The integrand  $r B_z(r)$  can be replaced using Eq. (2.98) to simplify the integral and

give

$$Q = \frac{2\pi L\sigma_H}{c} \frac{\omega^2}{\omega_L^2 - \omega^2} \int_{R_i}^{\infty} \frac{\partial(rE_\theta)}{\partial r} dr \quad (2.133)$$

$$= -i \frac{2\pi R_i L \sigma_H \omega}{\omega_L^2 - \omega^2} E_\theta(R_i), \quad (2.134)$$

where  $A_{R_i} = 2\pi R_i L$  is the area on the inner surface of the superconducting cylinder. The charge in the bulk is opposite to the charge on the inner surface of the superconductor, as one would expect:

$$Q_{R_i} = -Q. \quad (2.135)$$

We have seen that the details are similar whether the magnetic field comes from a solenoid outside or inside of the superconductor. The practical difference is that a solenoid inside the superconductor must be small. It would be difficult for an experimenter to obtain a high magnetic field in a small solenoid. On the other hand, a smaller solenoid has lower inductance and may make it easier to have a high-frequency ac current.

## 2.10 Conclusions

In this chapter, we considered the feasibility of testing a superconductor for TRSB by directly measuring the low-frequency Hall conductivity. This measurement would shed light on the controversy as to whether the spontaneous dc Hall effect exists in TRSB superconductors [15, 31, 38].

For theoretical clarity, we considered an infinite annular cylinder of superconducting material and showed that, if the cylinder is placed inside a magnetic field (or, equivalently, a solenoid with ac current), a circular electric field occurs as a part of Meissner screening. We showed that if there is Hall conductivity, then Hall current flows in the radial direction, causing a surface charge to accumulate at the boundary of the superconductor. This surface charge is compensated by radial supercurrent, leading to radial charge oscillations at the London frequency. We estimated the surface charge and Hall voltage across the inner and outer surfaces, which could be measured in an experiment.

Our schematic experiment used a conical waveguide attached to a coaxial cable to measure the potential difference across a Corbino disk. In order to develop an experimental estimate, we obtained a formula for Hall conductivity from a model of chiral d-wave superconductivity, and then provided a possible estimate for the Hall voltage in the nanovolt range. We argued that the intrinsic Hall effect produces a first harmonic response, while the extrinsic Hall effect would produce a second harmonic response. Consequently, the first harmonic response uniquely implies spontaneous Hall conductivity.

We also argue for an important difference between transverse Hall current and linear current. The linear supercurrent is oscillatory at the frequency  $\omega_L \approx \omega_p$  and the normal current is purely dissipative, while the Hall current is able to couple to the local electric field and drive charge oscillations. That bulk charge density oscillates at the frequency  $\omega_L$  was already expected for conventional superconductors [39], but to our knowledge has not been seen in experiment. Since prior work did not

consider the unique role of Hall current in driving charge oscillations, our work may provide guidance in locating the plasma oscillations in superconductors.



## Chapter 3: URu<sub>2</sub>Si<sub>2</sub> and Metastable Magnetism in the HO Phase

### 3.1 Introduction

The heavy-fermion material URu<sub>2</sub>Si<sub>2</sub> exhibits a second-order phase transition from paramagnetism to a puzzling hidden order (HO) phase at  $T_{\text{HO}} = 17.5$  K [40,41], where the corresponding symmetry breaking has not been definitively established. Particularly interesting is the question of whether time-reversal (TR) symmetry in the HO phase is preserved or broken. Raman spectroscopy gives evidence for the spontaneous breaking of mirror symmetries, so Kung *et al.* [1] interpreted HO as a chirality density wave that preserves TR symmetry (TRS). However, Schemm *et al.* [42] observed a non-zero polar Kerr effect (PKE) in the HO phase, indicating possible TRS breaking (TRSB)<sup>1</sup>. In this chapter, we attempt to reconcile the experimental results of Refs. 1 and 42 within a unified theoretical framework based on an earlier model of HO developed by Haule and Kotliar in Refs. 43,44.

According to Ref. 42, URu<sub>2</sub>Si<sub>2</sub> exhibits zero PKE when cooled without an applied magnetic field, which is consistent with TRS preservation in the HO phase.

However, when URu<sub>2</sub>Si<sub>2</sub> is cooled in a training magnetic field up to 2 T, which is then

---

<sup>1</sup>The primary focus of Ref. 42 was on TR symmetry breaking in the superconducting phase of URu<sub>2</sub>Si<sub>2</sub> below  $T_c = 1.5$  K, whereas our focus is on TR symmetry breaking in the HO phase, which was also studied in Ref. 42.

removed at low temperature, a non-zero PKE is observed on warm-up in the HO phase. Apparently, the external magnetic field induces magnetism in the material that is preserved even after the field has been removed. Schemm *et al.* [42] interpreted this persistent magnetism as extrinsic in origin, resulting from unspecified magnetic states due to strain or defects. While explanations due to sample inhomogeneity are possible [45–48], we advance an alternative proposition - that the induced magnetism is intrinsic to HO and would occur even in a perfectly uniform sample.

We approach this problem from the perspective of the Haule-Kotliar model [43, 44] characterized by a two-component complex order parameter. The real part represents chiral order consistent with the observations of Ref. 1, whereas the imaginary part represents magnetic order. Using a modified version of the associated free energy, we study the interplay and competition between the two components of the order parameter. We find that, when the system is cooled in a magnetic field, it may become trapped at a local minimum of the free energy, corresponding to a metastable ferromagnetic (FM) state and exhibiting the PKE. This conjecture of a metastable FM state is supported by the observation of hysteresis in direct magnetization measurements of single crystals of URu<sub>2</sub>Si<sub>2</sub> cooled in zero and non-zero fields [49].

Our proposition can be tested by applying a reversed magnetic field at low temperature. We predict that, when the reversed field exceeds a certain threshold, the system will make an irreversible transition from the metastable FM to the true HO ground state, thereby resetting the PKE (or magnetization) to zero. In contrast,

an extrinsic FM would change sign in a reversed magnetic field instead of being eliminated. An experimental verification of this prediction would be a crucial test of the metastable intrinsic FM scenario and would qualitatively discriminate it from other possible explanations of the induced PKE.

### 3.2 URu<sub>2</sub>Si<sub>2</sub>

URu<sub>2</sub>Si<sub>2</sub> is one of multiple U alloys that have been studied since the 1980s due to the unusual properties which result from the U-5*f* electron shell. For the U-5*f* electrons, the exchange interaction, the 5*f* bandwidth, the spin-orbit interaction, and the intra-atomic *f* – *f* Coulomb interaction are all on the same energy scale, leading to multiple interesting consequences [40]. The U-based compounds have intermediate behavior between that of transition metals and that of rare earth metals. They also have intermediate behavior between localized and itinerant 5*f* electrons. Additionally, there are multiple possible valences for the 5*f* electrons and there is a large spin-orbit coupling.

In URu<sub>2</sub>Si<sub>2</sub>, the 5*f* electrons are partially itinerant and partially reside in Ising-like magnetic moments [40]. The coexistence of local and itinerant electrons is related to the Kondo interaction between conduction electrons and the local moments, which enable the electron mass to have a renormalized value that is heavy [50]. The effective conduction electron masses vary from 10 to 25 times the electron mass [51]. Since the material evidences both itinerant and local electron phenomena, theories of HO are typically divided on whether HO is an itinerant or local phenomenon.

The symmetry breaking that occurs at  $T_{\text{HO}}$  has a large associated entropy,  $S = \int_0^{T_{\text{HO}}} (\Delta C/T) dT \approx 0.2R \ln 2$ , which is a sizable fraction of the ideal gas constant. In line with the antiferromagnetic phases that often exist in the uranium-based heavy-fermion materials, this phase transition was reported as magnetic. And in fact, X-ray scattering did reveal magnetic Bragg peaks corresponding to an antiferromagnetic structure, but the ordering magnetic moment was a very small fraction of the Bohr magneton,  $\mu = (0.03 \pm 0.01)\mu_B$  per uranium atom. This “small moment antiferromagnetism” was too small to explain the total entropy of the phase transition and made the HO order parameter very controversial.

A magnetic explanation for HO may seem tempting because other uranium-based heavy fermion compounds often have magnetic phases. Indeed, if we consider the pressure vs temperature phase diagram in Fig. 3.2, we can see there is an antiferromagnetic (AF) phase adjacent to the HO. Elastic neutron scattering at high pressure reveals the AF phase to have a magnetic order that is uniform within  $a - b$  plane layers, but staggered between adjacent layers in the  $c$  direction, thus doubling the unit cell along the  $c$  axis. This moment agrees with  $c$ -axis period doubling seen in the HO phase by ARPES measurements [52], and there is an “adiabatic continuity” between the HO and AF phases in which the resistivity changes continuously from the AF to the HO phase [53, 54]. On the other hand, neutron scattering and Si nuclear magnetic resonance (NMR) studies have suggested that the ordered moment is contained in small AF pockets that may exist within the HO phase [47, 55]. HO may respect TRS and only contain pockets of TRSB AF, since the two phases are separated by a first-order phase transition at high pressure [40]. These pockets may

be the result of defects, but it is also possible that the two phases are close enough in energy that they are metastable and may occur in a clean sample.

Although 600 papers have been published on  $\text{URu}_2\text{Si}_2$  with many different theories by dozens of authors, we focus on a particular conception of HO based on a localized  $5f^2$  electron configuration. With respect to the point group  $D_{4h}$  giving the symmetry of  $\text{URu}_2\text{Si}_2$ , potential wavefunctions can be decomposed into different representations of the group. An early crystalline electric field scheme reproduced some of the thermodynamic properties of HO by assuming that the two low-lying states had symmetries  $\Gamma_1^{(1)} = A_{1g}$  and  $\Gamma_2 = A_{2g}$  corresponding to “hexadecapolar order” [56, 57]. This scheme saw renewed attention due to a first-principles calculation by Haule and Kotliar using a combination of dynamic mean field theory and density functional theory to calculate the the local wavefunction of the  $5f^2$  electrons [43]. The calculation predicted an  $A_{2g}$  ground state and  $A_{1g}$  excited state, which can hybridize to produce the hexadecapolar order in the ground state. More intriguing still, Haule and Kotliar showed that in general the  $A_{2g}$ -valued hybridization of the two low-lying states produces a complex order parameter that can be hexadecapolar or dipolar [44]. They formulated a mean-field theory model for the complex order parameter and argued that both the HO and AF phases emerge as the real and imaginary parts of the same complex order parameter.

The  $A_{2g}$  complex order parameter gained further support from two Raman scattering experiments. The first experiment used polarized Raman spectroscopy to directly observe the symmetry of the transition between the low-lying states and a nearby conduction band [1]. They found broken  $A_{2g}$ , which can be understood

as the breaking of four vertical mirror planes, as depicted in Fig. 3.1 and discussed in the next section. They then argue that HO is a “chirality density wave”. The same group carried out a follow-up experiment in which a HO to AF transition was carried out in  $\text{URu}_{2-x}\text{Fe}_x\text{Si}_2$  by doping [58]. The  $A_{2g}$  Raman signal disappears at the transition from HO to AF and then reappears and increases with further doping. Since HO and AF are separated by a first-order phase transition, the disappearance and re-emergence of the signal is interpreted as a transition from a ground state where the order parameter is real to a ground state where the order parameter is imaginary. The chirality density wave is depicted in Fig. 3.1.

### 3.3 Haule-Kotliar Model

$\text{URu}_2\text{Si}_2$  is a body-centered tetragonal crystal, where uranium atoms are arranged in square-lattice layers perpendicular to the  $c$  axis. The crystal has a four-fold rotational symmetry about the  $c$  axis and four vertical mirror planes (VMP) through the  $c$  axis. According to Ref. 43, the  $5f^2$  electrons of the uranium atoms have the ground state  $|A_2\rangle = i(|4, 4\rangle - |4, -4\rangle)/\sqrt{2}$  and the lowest excited state  $|A_1\rangle = \cos\phi(|4, 4\rangle + |4, -4\rangle)/\sqrt{2} + \sin\phi|4, 0\rangle$ , written in the angular momentum basis  $|J, J_z\rangle$ , where the  $z$  axis is taken along the  $c$  axis, and  $\phi \approx 0.37\pi$ . Inelastic non-resonant X-ray spectroscopy supports the conjecture that  $|A_1\rangle$  and  $|A_2\rangle$  are indeed the low-lying states of the system [59].

A model Hamiltonian  $H$  consistent with both VMP and TR symmetries can be constructed [44] using Pauli matrices  $\{\sigma_j^x, \sigma_j^y, \sigma_j^z\}$  in the basis of  $|A_2\rangle_j$  and  $|A_1\rangle_j$

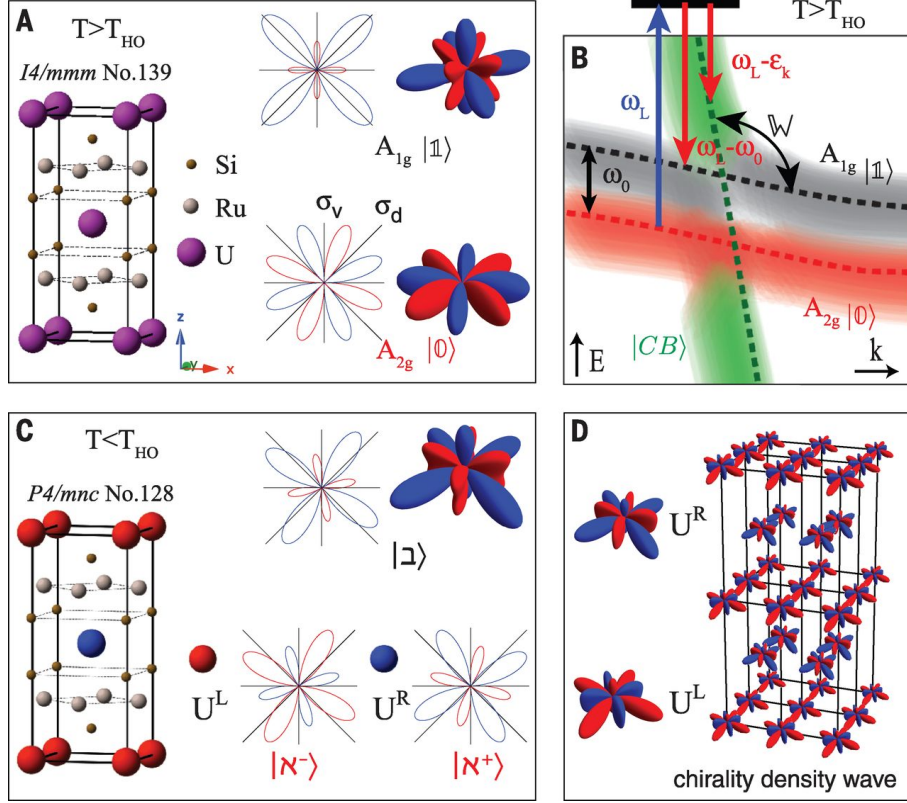


Figure 3.1: This figure shows the  $A_{2g}$  symmetry breaking of the local  $5f^2$  electron wavefunctions. (A) The crystal structure and wavefunctions are presented in the paramagnetic state. The high-temperature wavefunctions have two vertical mirror plane symmetries  $\sigma_v$  and  $\sigma_d$ . (B) A schematic band structure of the low-lying states and conduction band is shown. (C) The crystal structure remains the same below the transition temperature, but the hybridized wavefunctions break the vertical mirror plane symmetries and pick up chirality. (D) An antiferromagnetic ordering of chiralities is shown, indicating a chirality density wave. Figure from Ref. 1. Reprinted with permission from AAAS.

at each uranium site labeled by coordinate  $j$ :

$$H = \sum_{\langle j,k \rangle} [J_{jk}^x \sigma_j^x \sigma_k^x + J_{jk}^y \sigma_j^y \sigma_k^y] - \sum_j [\Delta \sigma_j^z + b \sigma_j^y]. \quad (3.1)$$

Here  $2\Delta = 35$  K is the energy splitting of the  $A_1$  and  $A_2$  states<sup>2</sup>,  $b = \mu_{\text{eff}} B$  is the energy of interaction with an external magnetic field  $B$  applied along the  $c$  axis, and

<sup>2</sup>Our definition of  $\Delta$  differs by a factor of 2 from Ref. 44. We choose  $\Delta = 17.5$  K for consistency with Ref. 44.

the amplitudes  $J_{jk}^{x,y}$  describe interaction between the nearest neighboring sites  $\langle j, k \rangle$ . The Pauli matrices transform as  $\sigma^{x,y} \rightarrow -\sigma^{x,y}$  and  $\sigma^z \rightarrow \sigma^z$ , upon VMP reflections because  $|A_2\rangle$  is odd and  $|A_1\rangle$  is even. Thus, the first two terms in  $H$  are bilinear in  $\sigma^{x,y}$ , and the third term is linear in  $\sigma^z$ . Additionally,  $\sigma^y \rightarrow -\sigma^y$  upon TR due to complex conjugation, so  $\sigma^y$  couples linearly to the magnetic field in the last term.

At low temperature, the system described by Eq. (3.1) may undergo a phase transition that breaks VMP symmetries and results in hybridization of the even  $|A_1\rangle$  and odd  $|A_2\rangle$  states. It is characterized by the anomalous average

$$\psi_j = 2 \langle A_1 |_j \rho | A_2 \rangle_j = \text{Tr}[\rho(\sigma_j^x + i\sigma_j^y)] = \psi_j^x + i\psi_j^y, \quad (3.2)$$

where  $\rho$  is the density matrix, whereas  $\psi_j^x = \langle \sigma_j^x \rangle$  and  $\psi_j^y = \langle \sigma_j^y \rangle$  are the real and imaginary parts of the complex order parameter  $\psi_j$ . The real part represents HO and is equivalently characterized by a non-zero expectation value  $\psi_j^x = -\text{Tr}[\rho J_x J_y (J_x^2 - J_y^2)]/8 \cos \phi$  of the hexadecapolar operator [43], which is antisymmetric with respect to VMP reflections and symmetric with respect to TR. The associated ground state is a real superposition of  $|A_2\rangle_j$  and  $|A_1\rangle_j$  asymmetric with respect to VMP reflections, so it breaks chiral symmetry [1] but preserves TR symmetry. The imaginary part of the order parameter  $\psi_j^y = \text{Tr}[\rho J_z]/4 \cos \phi$  represents a magnetic moment along the  $c$  axis and is non-zero for a complex superposition of  $|A_2\rangle_j$  and  $|A_1\rangle_j$ . Below, we analyze the emergence of the chiral and magnetic orders using a mean-field theory.

In the mean-field approximation  $\sigma_n^\alpha \sigma_m^\beta \rightarrow \psi_n^\alpha \sigma_m^\beta + \sigma_n^\alpha \psi_m^\beta - \psi_n^\alpha \psi_m^\beta$ , the free



energy at temperature  $T = 1/\beta$  is given by

$$F = \sum_j \gamma (\psi_j^x \psi_j^y)^2 - T \ln [\cosh (\beta \lambda_j)] - \sum_{\substack{\langle j,k \rangle \\ \alpha=x,y}} J_{jk}^\alpha \psi_j^\alpha \psi_k^\alpha$$

$$\lambda_j = \sqrt{\Delta^2 + \left( \sum_k J_{jk}^x \psi_k^x \right)^2 + \left( \sum_k J_{jk}^y \psi_k^y - b \right)^2}. \quad (3.3)$$

Here we have introduced the additional term  $\gamma(\psi_j^x \psi_j^y)^2$  with  $\gamma > 0$  to discourage on-site co-existence of the chiral and magnetic orders, which is necessary to account for the first-order phase transition between HO and antiferromagnetism (AF) under pressure [40].

Elastic neutron scattering in the high-pressure AF phase [60, 61] reveals a magnetic order that is uniform within layers, but staggered between adjacent layers, thus doubling the unit cell along the  $c$  axis. A similar  $c$ -axis period doubling is also discussed for the HO phase, based on ARPES measurements [52] and the “adiabatic continuity” between the HO and AF phases seen in resistivity studies [53, 54]. Therefore, we take HO to be staggered,  $\psi_n^x = (-1)^n \psi_{\text{HO}}$ , as a function of the layer number  $n$ , in agreement with the notion of a chirality density wave [1]. Similarly, we decompose the magnetic order into the uniform and staggered components,  $\psi_n^y = \psi_{\text{FM}} + (-1)^n \psi_{\text{AF}}$ , representing FM and AF. Then, we rewrite Eq. (3.3) in terms of the three order parameters  $\psi_{\text{HO}}$ ,  $\psi_{\text{AF}}$ , and  $\psi_{\text{FM}}$  coupled to the effective interaction constants  $J_\pm^\alpha = -(4J_\parallel^\alpha \pm 8J_\perp^\alpha)$ , where  $J_\parallel^\alpha < 0$  and  $J_\perp^\alpha > 0$  are the intralayer and interlayer values of  $J_{ij}^\alpha$ . Positive values of the interaction amplitudes  $J_-^x > J_-^y > J_+^y > 0$  favor HO over AF over FM.

### 3.4 Competition of Hidden Order and Antiferromagnetism

Equation (3.3) was used in Ref. 44 to study the interplay between HO and AF as a function of pressure in the absence of magnetic field. In this case  $\psi_{\text{FM}} = 0$ , and free energy per site  $f = F/N$  ( $N$  is the site count) is

$$f[\psi_{\text{HO}}, \psi_{\text{AF}}] = J_-^x \psi_{\text{HO}}^2 + J_-^y \psi_{\text{AF}}^2 + \gamma \psi_{\text{HO}}^2 \psi_{\text{AF}}^2 - T \ln \left[ \cosh \left( \beta \sqrt{\Delta^2 + (J_-^x \psi_{\text{HO}})^2 + (J_-^y \psi_{\text{AF}})^2} \right) \right]. \quad (3.4)$$

Let us examine how the energy landscape given by Eq. (3.4) changes with the decrease of temperature for points A, B, and C on the schematic phase diagram in Fig. 3.2. In Figs. 3.3(a)-(c) we show contour plots of  $f[\psi_{\text{HO}}, \psi_{\text{AF}}]$  vs.  $\psi_{\text{HO}}$  on the horizontal axis and  $\psi_{\text{AF}}$  on the vertical axis. The red arrows in Fig. 3.3 indicate the state of the system during the described evolution. At point A for  $T > T_{\text{HO}}$ , the system is at the energy minimum  $\psi_{\text{HO}} = \psi_{\text{AF}} = 0$  as shown in Fig. 3.3(a). At point B for  $T = 15.3 \text{ K} < T_{\text{HO}}$ , the minimum at the origin splits into two degenerate minima on the horizontal axis shown in Fig. 3.3(b). Consequently, the system spontaneously breaks symmetry and acquires  $\psi_{\text{HO}} \neq 0$  via a second-order phase transition. Using the condition  $\partial^2 f / \partial \psi_{\text{HO}}^2 = 0$  at  $\psi_{\text{HO}} = \psi_{\text{AF}} = 0$  for the transition temperature  $T_{\text{HO}} = 17.5 \text{ K}$ , the interaction constant  $J_-^x = 2\Delta / \tanh(\Delta/T_{\text{HO}}) \approx 46 \text{ K}$  can be deduced [44]. At a lower temperature, such as  $T = 3 \text{ K}$  for point C, the free energy develops a second pair of shallower (local) minima along the vertical (magnetic) axis as shown in Fig. 3.3(c), but the system stays at one of the global

minima with  $\psi_{\text{HO}} \neq 0$  and  $\psi_{\text{AF}} = 0$ . Under pressure, the AF minima on the vertical axis become deeper than the non-magnetic minima on the horizontal axis, so the system undergoes a first-order phase transition from HO to AF with  $\psi_{\text{AF}} \neq 0$  and  $\psi_{\text{HO}} = 0$  at high pressure [44]. To explain the first order of the phase transition, we choose a large enough  $\gamma \approx 64$  K to ensure an energy barrier separating the minima on the magnetic and non-magnetic axes. This picture is supported by Raman spectroscopy [58] in Fe-doped URu<sub>2</sub>Si<sub>2</sub>, where optically-induced transitions between the HO and AF minima in the energy landscape were observed. Using the value  $T_{\text{AF}} = 15$  K extrapolated to ambient pressure [44] and its associated condition  $\partial^2 f / \partial \psi_{\text{AF}}^2 = 0$  at the origin, we deduce  $J_-^y = 2\Delta / \tanh(\Delta/T_{\text{HO}}) \approx 43$  K.

### 3.5 Competition of Hidden Order and Ferromagnetism

A staggered AF order does not explain the field-induced PKE observed in Ref. 42, because it cannot be trained by a uniform magnetic field, and the contributions from alternating layers cancel out. So, we turn our attention to non-staggered FM order  $\psi_{\text{FM}}$ . The training magnetic field  $B$  couples to it linearly in Eq. (3.1), thus lowering the energy of the FM state and making it competitive with HO. In contrast, AF has higher energy than HO at ambient pressure, so we set  $\psi_{\text{AF}} = 0$ , and the free energy per site in Eq. (3.3) becomes

$$f[\psi_{\text{HO}}, \psi_{\text{FM}}] = J_-^x \psi_{\text{HO}}^2 + J_+^y \psi_{\text{FM}}^2 + \gamma \psi_{\text{HO}}^2 \psi_{\text{FM}}^2 - T \ln \left[ \cosh \left( \beta \sqrt{\Delta^2 + (J_-^x \psi_{\text{HO}})^2 + (J_+^y \psi_{\text{FM}} + b)^2} \right) \right]. \quad (3.5)$$

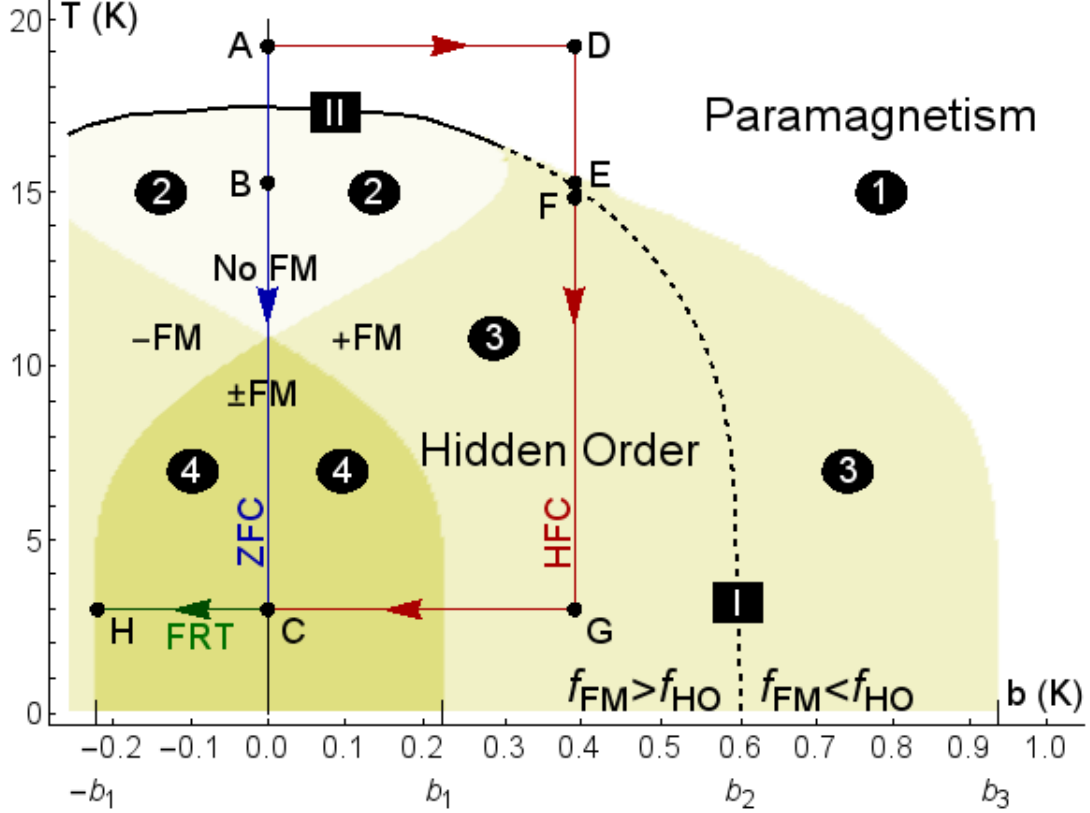


Figure 3.2: Phase diagram for the free energy in Eq. (3.5) as a function of magnetic energy  $b$  and temperature  $T$ . The numbers in circles and the degree of shading indicate the number of minima of  $f[\psi_{\text{HO}}, \psi_{\text{FM}}]$ . Every shaded domain has two degenerate HO minima with  $|\psi_{\text{HO}}| \neq 0$  and may have one or two FM minima with  $\psi_{\text{FM}} > 0$  or  $\psi_{\text{FM}} < 0$ , as schematically indicated around  $T = 10$  K. The HO (FM) minima have lower energy to the left (right) of the dashed first-order transition line labeled I. The solid line labeled II represents a second-order phase transition from paramagnetism to HO. Blue, red, and green lines represent the Zero-Field Cooling (ZFC), High-Field Cooling (HFC), and Field-Reversal Test (FRT) protocols.

Eq. (3.5) differs from Eq. (3.4) by the coefficient  $J_-^y \rightarrow J_+^y$  and the presence of magnetic energy  $b$ . The difference between  $J_+^y$  and  $J_-^y$  is only due to the small interlayer coupling  $J_{\perp}^y$ , so  $J_+^y$  still has a positive sign favorable for FM. Since the value of  $J_{\perp}^y$  is unknown, we take  $J_+^y \approx 43$  K as an estimate. The observation of a FM phase in Re, Tc, and Mn doped samples [62–65] indicates that FM can, indeed, be a close competitor of HO.

Let us compare two experimental protocols employed in Ref. 42 for going from

point A to point C in Fig. 3.2: zero-field cooling (ZFC) via A-B-C and high-field cooling (HFC) via A-D-E-F-G-C. The energy landscape of Eq. (3.5) at points A, B, and C is shown in Fig. 3.3(a)-(c) and has already been discussed below Eq. (3.4), but now the vertical axis represents  $\psi_{\text{FM}}$  instead of  $\psi_{\text{AF}}$ . During ZFC, the system undergoes a second-order phase transition to the HO ground state with  $\psi_{\text{HO}} \neq 0$  and  $\psi_{\text{FM}} = 0$ , and stays there as temperature decreases.

Now let us consider HFC starting at point A, where the energy minimum is located at  $\psi_{\text{HO}} = \psi_{\text{FM}} = 0$  as shown in Fig. 3.3(a). Next, a training magnetic field  $b = 0.4$  K is applied (point D in Fig. 3.2) shifting the energy minimum in the FM direction  $\psi_{\text{FM}} > 0$  as shown in Fig. 3.3(d). At point E with  $T = 15.3$  K, the free energy develops two shallow degenerate HO minima, but the system stays in the pre-existing FM global minimum as shown in Fig. 3.3(e). At nearby point F with  $T = 15$  K, the HO minima become deeper than the FM minimum as seen in Fig. 3.3(f), but the energy barriers prevent a transition. So, the system stays in the metastable FM minimum all the way down to  $T = 3$  K at point G, as shown in Fig. 3.3(g). Removing the magnetic field at  $T = 3$  K takes the system to point C in Fig. 3.2 while preserving its FM state as depicted in Fig. 3.3(h). Although the energy landscape in panel (h) is exactly the same as in panel (c), the state of the system is different: It is HO for ZFC and FM for HFC. The metastable FM state is reached because HFC crosses the first-order rather than the second-order phase transition line in Fig. 3.2. Finally, when temperature is increased along the path C-B-A at  $b = 0$ , the FM metastable state exhibits a non-zero PKE, as observed on warmup at zero field in Ref. 42.

The theoretical scenario presented above offers a qualitative explanation of experiment [42] but has shortcomings. First, the experimental PKE persists on warmup to  $T > T_{\text{HO}}$ , whereas in our model the FM minimum in free energy disappears at  $T < T_{\text{HO}}$ . Second, the PKE magnitude observed in Ref. [42] increases with the increase of the training magnetic field. This feature can be explained theoretically by considering partial statistical population of different states in the energy landscape due to thermal fluctuations. However, further refinements of the model are beyond the scope of this chapter and are left for future studies.

### 3.6 Field-Reversal Test

The proposed scenario can be tested by applying a reversed magnetic field, in the opposite direction relative to the HFC training field, at low temperature. When the magnetic energy reaches a critical magnitude  $-b_1 \approx -0.22$  K corresponding to point H in Fig. 3.2, the metastable FM minimum transforms into a saddle point as shown in Fig. 3.3(i), so the system makes an irreversible transition to one of the HO minima indicated by the red arrows. This transition can be detected by applying and removing a progressively increasing reversed magnetic field at low temperature, while measuring the PKE at  $b = 0$  in each cycle.

Instead of using the optical PKE technique, the metastable FM can also be observed by direct magnetization measurements [49] using a sensitive probe, such as a SQUID magnetometer. The magnetic moment in the FM state can be crudely estimated to be of the same order as the staggered magnetic moment  $m_{\text{AF}} = 0.3\mu_B$

experimentally measured [61] in the AF phase. However, the magnetic moment in the metastable FM state would be greatly reduced by thermal fluctuations between the global and local minima in Fig. 3.3. Therefore, the effective FM moment is expected to be small, so that direct measurement of magnetization would require high sensitivity, consistent with the PKE sensitivity. The field-reversal test of the metastable FM state can also be performed using direct magnetization measurements.

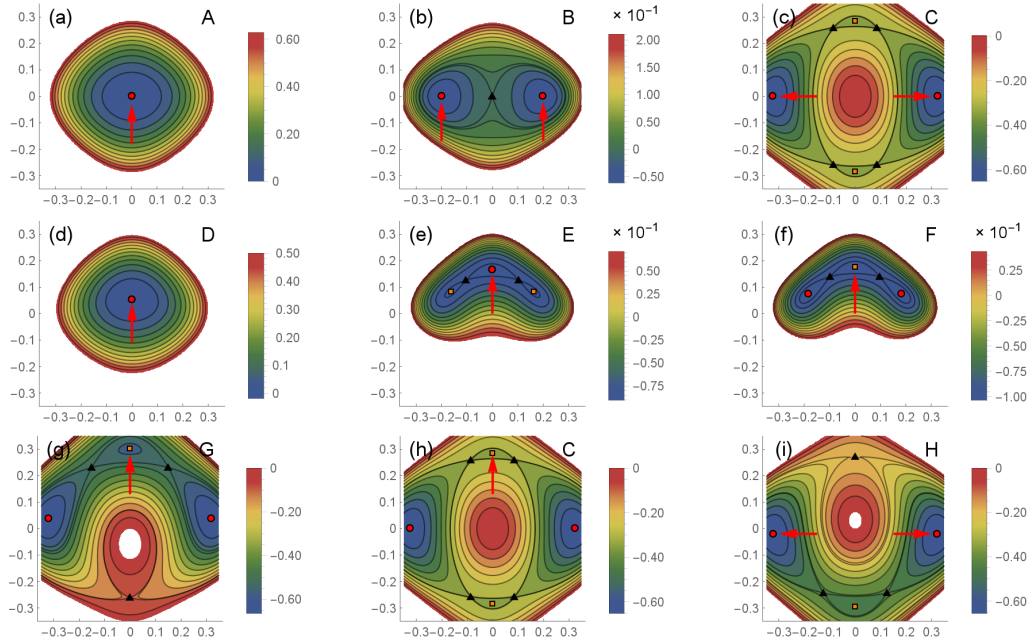


Figure 3.3: Contour plots of the free energy  $f[\psi_{HO}, \psi_{AF}]$  given by Eq. (3.4) or  $f[\psi_{HO}, \psi_{FM}]$  given by Eq. (3.5) for points A-H in Fig. 3.2. The horizontal and vertical axes represent the non-magnetic,  $\psi_{HO}$ , and magnetic,  $\psi_{AF}$  for (a)-(c) and  $\psi_{FM}$  for (a)-(i), components of the order parameter. Global minima, local minima, and saddle points are indicated by red disks, orange squares, and black triangles, while red arrows indicate the state of the system reached following the paths in Fig. 3.2.

### 3.7 Comparison with Experiment

The magnetic energy  $b_1$  in the field-reversal test is one of the several characteristic magnetic energies  $b_1, b_2, b_3$  shown in Fig. 3.2, indicating qualitative changes in the free-energy landscape in Fig. 3.3. The magnetic energy  $b_2$  corresponds to the first-order phase transition between  $\psi_{\text{HO}}$  and  $\psi_{\text{FM}}$ , where the free energy  $f_{\text{HO}}$  of the HO minima in Fig. 3.3 is equal to the free energy  $f_{\text{FM}}$  of the FM minimum. The magnetic energy  $b_3$  corresponds to the termination of the metastable HO phase, where the HO minima in Fig. 3.3 disappear. Experimentally, HO terminates at a magnetic field of about 35 T [66]. For comparison of theory with experiment, we need to convert magnetic energy  $b$  in Kelvins into magnetic field  $B$  in Teslas. The conversion coefficient can be estimated as  $B/b = \mu_{\text{eff}}^{-1} = 1.2 \text{ T/K}$  using the effective magnetic moment  $\mu_{\text{eff}} = |\langle A_2 | L_z + 2S_z | A_1 \rangle| \mu_B = 1.25\mu_B$  quoted in Ref. 44. However, for  $b_3 = 0.93 \text{ K}$  in Fig. 3.2, this  $\mu_{\text{eff}}$  gives the terminating field  $B_3 = 1.1 \text{ T}$ , which is far short of the 35 T seen in experiment. This discrepancy can be resolved in two ways.

The value  $b_3 = 0.93 \text{ K}$  shown in Fig. 3.2 was obtained for particular values of the unknown parameters  $\Delta, J_+^y$ , and  $\gamma$  and can be increased by adjusting those parameters. A formula for  $b_3$  is derived in section (3.8), and the maximal value  $b_3^{(\text{max})} = T_{\text{HO}}$  is achieved in the limit  $\gamma \rightarrow \infty$  and  $\Delta \rightarrow 0$ . Using  $\mu_{\text{eff}}^{-1} = 1.2 \text{ T/K}$  and  $b_3^{(\text{max})} = T_{\text{HO}} = 17.5 \text{ K}$ , we obtain  $B_3 = 21 \text{ T}$ , which is closer to the experimental value.

Moreover, the conversion coefficient  $\mu_{\text{eff}}$  can be estimated from experiment,



rather than from the theoretical quote in Ref. 44. The staggered moment observed in the antiferromagnetic phase in experiment [61] is  $m_{\text{AF}} = 0.3\mu_B$  per uranium atom. Comparing with the theoretical formula in Eq. (3.17) computed in section 3.9, we find  $\mu_{\text{eff}} = 0.3\mu_B$  in the limit  $\Delta \rightarrow 0$ , which is four times lower than the prior estimate. Combining this estimate for  $\mu_{\text{eff}}$  with the estimate for the maximal  $b_3^{(\text{max})} = T_{\text{HO}} = 17.5$  K, we obtain  $B_3 = 87$  T, which exceeds 35 T by a wide margin. It shows that the theoretical estimate of the HO terminating magnetic field can be made large enough to match experiment by tuning the parameters of the model.

For illustration we repeat the calculation for alternative values  $\Delta = 7$  K and  $\gamma = 525$  K and the corresponding generated values of  $J_-^x = 2\Delta/\tanh(\Delta/T_{\text{HO}}) = 37$  K,  $J_+^y = J_-^y = 2\Delta/\tanh(\Delta/T_{\text{AF}}) = 32$  K, and  $\mu_{\text{eff}} \approx 0.33\mu_B$ . The new phase diagram, shown in Fig. 3.4, shares qualitative features with Fig. 3.2, but the characteristic energies  $b_1$  and  $b_2$  are interchanged. The HO termination energy  $b_3 = 6$  K translates into  $B_3 = 27$  T, and the field-reversal energy  $b_1 = 4$  K translates into  $B_1 = 18$  T.

So, there is a wide range of possible values for the characteristic fields  $B_1$  and  $B_3$  depending on the model parameters. However, the phase diagram of URu<sub>2</sub>Si<sub>2</sub> in a strong magnetic field is complicated with multiple phase transitions [67–69] not captured by our simple model. Additionally, the applicability of the Haule-Kotliar framework in very strong fields is not clear, as the basis states may change. So, our model should be primarily considered a qualitative, rather than quantitative, guide to experiment.

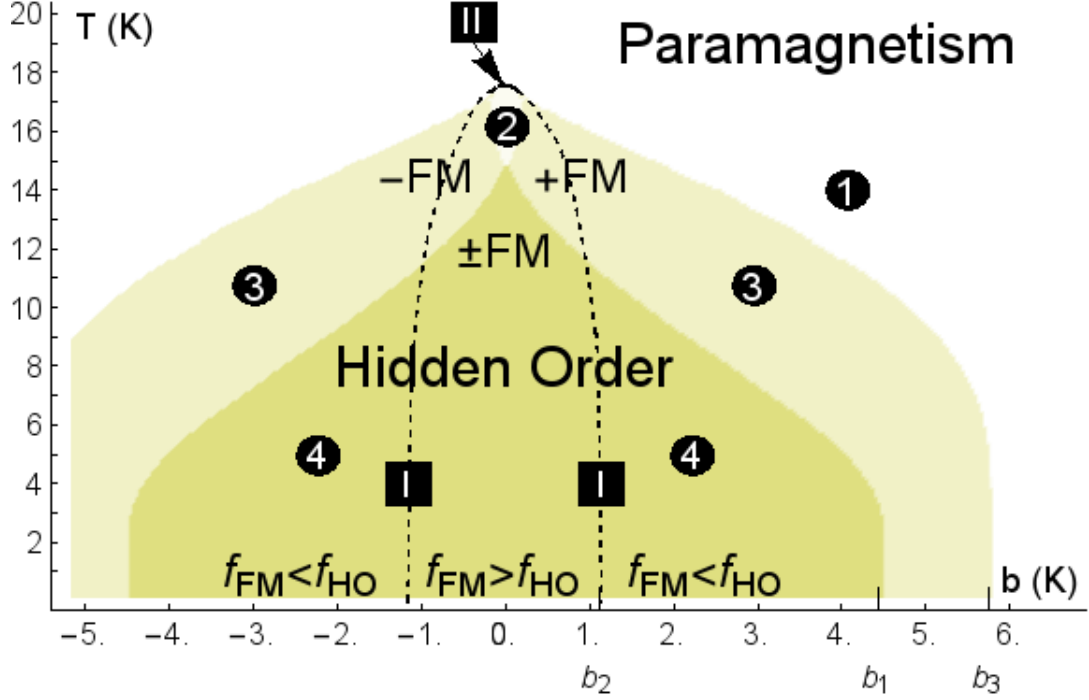


Figure 3.4: Phase diagram as in Fig. 3.2 recalculated using  $\Delta = 7$  K and  $\gamma = 525$  K (in contrast to  $\Delta = 35$  K and  $\gamma = 64$  K in Fig. 3.2). Notice the greater scale for the magnetic energy  $b$ .

### 3.8 The magnetic field terminating hidden order

Here we evaluate the critical magnetic field energy  $b_3$  corresponding to the termination of HO at  $T = 0$  on the phase diagrams shown in Figs. 3.2 and 3.4. It can be derived from the free energy in Eq. (3.5) at  $T = 0$ ,

$$f[\psi_{\text{HO}}, \psi_{\text{FM}}] = J_-^x \psi_{\text{HO}}^2 + J_+^y \psi_{\text{FM}}^2 + \gamma \psi_{\text{HO}}^2 \psi_{\text{FM}}^2 - \sqrt{\Delta^2 + (J_-^x \psi_{\text{HO}})^2 + (J_+^y \psi_{\text{FM}} + b)^2}. \quad (3.6)$$

A general consideration is somewhat complicated, so we study the limiting cases of  $\gamma = 0$  and  $\gamma \rightarrow \infty$ .

The case of  $\gamma = 0$  corresponds to the Haule-Kotliar model of Ref. 44, but we arrive at a different result for  $b_3$ . At  $\gamma = 0$ , minimization of the free energy in Eq. (3.6) gives two equations  $\partial f/\partial\psi_{\text{HO}} = \partial f/\partial\psi_{\text{FM}} = 0$ :

$$2\psi_{\text{HO}} = \frac{J_-^x \psi_{\text{HO}}}{\sqrt{\Delta^2 + (J_-^x \psi_{\text{HO}})^2 + (J_+^y \psi_{\text{FM}} + b)^2}}, \quad (3.7)$$

$$2\psi_{\text{FM}} = \frac{J_+^y \psi_{\text{FM}} + b}{\sqrt{\Delta^2 + (J_-^x \psi_{\text{HO}})^2 + (J_+^y \psi_{\text{FM}} + b)^2}}. \quad (3.8)$$

From Eq. (3.7) we find

$$2\sqrt{\Delta^2 + (J_-^x \psi_{\text{HO}})^2 + (J_+^y \psi_{\text{FM}} + b)^2} = J_-^x, \quad (3.9)$$

and then from Eq. (3.8) we find  $\psi_{\text{FM}} = b/(J_-^x - J_+^y)$ . The HO vanishes at the termination field  $b = b_3$ , where  $\psi_{\text{HO}} = 0$ . Using these values for  $\psi_{\text{HO}}$  and  $\psi_{\text{FM}}$  in Eq. (3.9), we find a formula for  $b_3$ :

$$b_3(\gamma = 0) = \frac{J_-^x - J_+^y}{2} \sqrt{1 - \left(\frac{2\Delta}{J_-^x}\right)^2}. \quad (3.10)$$

Eq. (3.10) replaces an incorrect formula on page 3 of Ref. 44 for the critical field  $b_c$  corresponding to our  $b_3$ . The formula in Ref. 44 gives  $b_c \propto J_-^x + J_+^y$ , which cannot be valid, because a correct formula must give  $b_3 \rightarrow 0$  in the limit  $J_-^x \rightarrow J_+^y$ , where an infinitesimal magnetic field would be necessary to favor FM over HO.

In the case  $\gamma \rightarrow \infty$ , the term  $\gamma\psi_{\text{HO}}^2\psi_{\text{FM}}^2$  in Eq. (3.6) imposes a high energy penalty for the co-existence of  $\psi_{\text{HO}}$  and  $\psi_{\text{FM}}$ , so we set  $\psi_{\text{FM}} = 0$ . Using this value

and  $\psi_{\text{HO}} = 0$  in Eq. (3.9), we find

$$b_3(\gamma \rightarrow \infty) = \frac{J_-^x}{2} \sqrt{1 - \left(\frac{2\Delta}{J_-^x}\right)^2} = \frac{\Delta}{\sinh(\frac{\Delta}{T_{\text{HO}}})}, \quad (3.11)$$

where the second equality follows from  $2\Delta/J_-^x = \tanh(\Delta/T_{\text{HO}})$ .

Comparing Eqs. (3.10) and (3.11), we observe that the highest termination field is achieved in our model in the limit  $\gamma \rightarrow \infty$  and  $\Delta \rightarrow 0$ , where Eq. (3.11) gives

$$b_3^{(max)} = T_{\text{HO}}. \quad (3.12)$$

### 3.9 The Staggered Magnetic Moment

Here we evaluate the staggered magnetic moment in the antiferromagnetic phase under pressure. We introduce a local magnetic field  $b_j$ , so that the free energy is given by Eq. (3.3) with  $b \rightarrow b_j$ . The local on-site magnetic moment  $m_j$  at  $b_j = 0$  and  $T = 0$  is given by

$$m_j = -\frac{\partial F}{\partial B_j} = -\mu_{\text{eff}} \frac{\partial F}{\partial b_j} = \quad (3.13)$$

$$= \mu_{\text{eff}} \frac{(\sum_k J_{jk}^y \psi_k^y)}{\sqrt{\Delta^2 + (\sum_k J_{jk}^x \psi_k^x)^2 + (\sum_k J_{jk}^y \psi_k^y)^2}}. \quad (3.14)$$

In the antiferromagnetic phase, we have  $\psi_n^y = (-1)^n \psi_{\text{AF}}$  and  $\psi_n^x = 0$ , so the staggered magnetic moment is  $m_n = (-1)^n m_{\text{AF}}$  where

$$m_{\text{AF}} = \mu_{\text{eff}} \frac{J_-^y \psi_{\text{AF}}}{\sqrt{\Delta^2 + (J_-^y \psi_{\text{AF}})^2}}. \quad (3.15)$$

Using the minimum condition  $\partial f/\partial\psi_{\text{AF}} = 0$  for  $f$  in Eq. (3.4) at  $T = 0$ , we find

$$\psi_{\text{AF}} = \sqrt{1 - \left(\frac{2\Delta}{J_-^y}\right)^2} \quad (3.16)$$

and

$$m_{\text{AF}} = \mu_{\text{eff}} \sqrt{1 - \left(\frac{2\Delta}{J_-^y}\right)^2} = \frac{\mu_{\text{eff}}}{\cosh(\Delta/T_{\text{AF}})}. \quad (3.17)$$

where we have used  $2\Delta/J_-^y = \tanh(\Delta/T_{\text{AF}})$ .

The formula for the staggered magnetic moment  $m_{(0,0,1)}$  given on page 3 of Ref. 44 differs from our Eq. (3.17) by an extra factor of 1/2, which we believe is incorrect.

### 3.10 Conclusions

We have proposed a theoretical scenario reconciling the TR invariance of the HO state with observation of a non-zero magnetic-field-induced PKE [42]. Competition between the real and imaginary parts of a complex order parameter in a generalized Haule-Kotliar model [44] results in either ground-state HO or metastable FM, depending on the path taken through the phase diagram. Our theory can be tested by applying a strong enough reversed magnetic field at low temperature, which should trigger a transition from FM to HO and cause the PKE to vanish. Although some issues remain open in our scenario, it has the advantage of giving a unified description of the HO and FM states within a single theoretical model

without invoking extrinsic effects.

In principle, the general approach presented in this chapter can be adapted to other two-level models of HO in the literature. In particular, the hastatic order proposed in Refs. [70](#), [71](#) is based on the  $5f^3$  configuration described by the effective spin  $1/2$  and could also be used to explain intrinsic magnetism. However, the hastatic model predicts an in-plane magnetic moment in the HO phase which is not observed experimentally [[72](#), [73](#)].

A non-zero PKE is also observed in the superconducting phase of  $\text{URu}_2\text{Si}_2$  [[42](#)] emerging from the HO phase below  $T_c = 1.5$  K. A generalized model for the two separate TR symmetry breakings in the HO and superconducting phases, independently controllable by a training magnetic field [[42](#)], remains a challenge for future study.

## Chapter 4: Majorana Modes in Bi/Ni Bilayers

### 4.1 Introduction

In a recent report it has been seen that superconducting Bi/Ni bilayers exhibit the PKE signal characteristic of TRSB [24](see Chapter 1). The Kerr signal is reported for a sample with Bi (25 nm)/Ni (2 nm) that is first cooled at zero magnetic field and then measured on warm-up in zero magnetic field. The onset of ZF Kerr signal occurs at the superconducting transition temperature  $T_c = 4.1$  K and reaches  $\theta_K \approx 120$  nrad at low temperature. The authors argue the signal emerges from superconductivity and not from the Ni magnetic moments. Since the Ni moments are parallel to the surface, they do not couple to the PKE probe. Also, the strength of the signal is stronger with increasing opacity of the Bi layer. Finally, the ferromagnetic Curie temperature of Ni is 400 K, which is much greater than the  $T_c$  at which the effect appears.

The authors of the Bi/Ni study [24] then discuss a possible superconducting condensate  $f(\mathbf{p}) = \langle \phi_{\mathbf{p}} \tilde{\phi}_{\mathbf{p}} \rangle$  between the Fermion field  $\phi_{\mathbf{p}}$  and its partner under time-reversal,  $\tilde{\phi}_{\mathbf{p}} = \nu_{\mathbf{p}}^* \phi_{-\mathbf{p}}$  ( $\nu_{\mathbf{p}}$  is a phase factor s.t.  $\nu_{\mathbf{p}} \nu_{-\mathbf{p}} = -1$ ). Such a pairing must be

even in momentum  $\mathbf{p}$  due to the behavior of the Fermion fields under time-reversal,

$$f(\mathbf{p}) = \langle \phi_{\mathbf{p}} \tilde{\phi}_{\mathbf{p}} \rangle = \nu_{-\mathbf{p}} \nu_{\mathbf{p}}^* \langle \tilde{\phi}_{-\mathbf{p}} \phi_{-\mathbf{p}} \rangle \quad (4.1)$$

$$= -\nu_{-\mathbf{p}} \nu_{\mathbf{p}}^* \langle \phi_{-\mathbf{p}} \tilde{\phi}_{-\mathbf{p}} \rangle = \langle \phi_{-\mathbf{p}} \tilde{\phi}_{-\mathbf{p}} \rangle = f(-\mathbf{p}). \quad (4.2)$$

Consequently, the TRS paired condensate must be even in the pairing momentum. Expanding in 2D harmonics  $f(\mathbf{p}) = \sum_m e^{im\theta_p} f_m$ , they argue that since the  $m = 0$  component is TRS and the  $m = \pm 1$  component is forbidden, then  $m = \pm 2$ , which corresponds to d-wave superconductivity, is a natural candidate to explain the TRSB superconductivity in Bi/Ni. Based on the symmetry of the crystal, they argue for a  $d_{xy} \pm id_{x^2-y^2}$  superconductivity state.

If Bi/Ni is a  $d+id$  superconductor, then it is a rare example of a 2D topological superconductor that may have topologically protected edge modes. In particular, it may have topologically protected Majorana zero-energy modes around half-quantum vortices. A Majorana operator  $\hat{\gamma}$  has the property  $\hat{\gamma}^\dagger = \gamma$ . A prior work found that vortices in a spin-singlet  $d_{xy} + id_{x^2-y^2}$  superconductor have no zero-energy bound state [74]. However, our case is different because we consider spin-orbit coupling and a Zeeman magnetic in addition to  $d_{xy} + id_{x^2-y^2}$  superconductivity, and we show that a Majorana zero-mode can exist around a vortex. To do this, we set up the problem to follow the argument of Sau et al. [75] for Majorana zero-modes in the topological s-wave superconductor. The structure of their argument is qualitative similar to the work by Gurarie and Radzihovsky [76], in which a Majorana bound state is shown to exist for a chiral p-wave superconductor. In the following sections,



we set up and solve the Bogoliubov de Gennes (BdG) equation for the topological  $d_{xy} + id_{x^2-y^2}$  system and then show that a Majorana zero mode can exist.

## 4.2 Majorana Quasiparticles

Supposing a superconducting condensate exists, then we can represent it with a quadratic mean-field theory (as discussed in chapter 1). We assume the standard Majorana mode ingredients of spin-orbit coupling and Zeeman splitting are present in the single particle Hamiltonian

$$H_0 = \eta p^2 + \alpha(\vec{\sigma} \times \vec{p}) \cdot \hat{z} + V_z \sigma_z - \mu \quad (4.3)$$

where  $V_z$  gives the Zeeman splitting,  $\alpha$  gives spin-orbit coupling, and  $\eta = 1/2m^*$  gives effective mass of the superconducting electrons. The  $d + id$  superconducting order parameter near an  $n$ -fold vortex is given by

$$\Delta_n(\mathbf{r}) = \sqrt{\Delta_0 \exp(i\theta n/2)} \frac{\Delta_0}{p_F^2} (p_x + ip_y)^2 \sqrt{\Delta_0 \exp(i\theta n/2)}. \quad (4.4)$$

The quadratic Hamiltonian for the 2D superconductor can be written in BdG form in terms of electron field operators  $c_\sigma(z)$ ,

$$\hat{H} = \int d^2\mathbf{r} \begin{bmatrix} c^\dagger(\mathbf{r}) \\ c(\mathbf{r}) \end{bmatrix}^\dagger \begin{bmatrix} H_0 & \Delta \\ \Delta^* & -H_0^* \end{bmatrix} \begin{bmatrix} c^\dagger(\mathbf{r}) \\ c(\mathbf{r}) \end{bmatrix} \quad (4.5)$$

where  $c(\mathbf{r})^\dagger = [c_\uparrow^\dagger(\mathbf{r}), c_\downarrow^\dagger(\mathbf{r})]$ .

In general, the excitations of a quadratic Hamiltonian are given in terms of Bogoliubov quasiparticle operators, but we're interested specifically in a Majorana excited state of the form

$$\gamma^\dagger = \int d^2\mathbf{r} \sum_{\sigma} [u_{\sigma}c^\dagger(z) + v_{\sigma}c(z)] \quad (4.6)$$

which acts on the ground state of the system  $|\Phi_0\rangle$  to create a state of equal energy,

$$\hat{H}\gamma^\dagger|\Phi_0\rangle = \gamma^\dagger\hat{H}|\Phi_0\rangle. \quad (4.7)$$

This condition for a zero-energy excitation can be rewritten as the BdG equation for a zero-energy state,

$$\begin{bmatrix} H_0(\mathbf{r}) & \Delta(\mathbf{r}) \\ \Delta^*(\mathbf{r}) & -\mathbb{T}^\dagger H_0 \mathbb{T} \end{bmatrix} \boldsymbol{\Phi}(\mathbf{r}) = 0, \quad (4.8)$$

where  $\boldsymbol{\Phi}(\mathbf{r}) = [u_\uparrow(\mathbf{r}), u_\downarrow(\mathbf{r}), v_\downarrow(\mathbf{r}), -v_\uparrow(\mathbf{r})]$  is a wavefunction for the bound state in the Nambu spinor basis and  $\mathbb{T} = i\sigma_y K$  is the time-reversal operator. The first two components of the Nambu spinor represent the ‘electron sector’ wavefunction and the latter two parts are the ‘hole sector’ (which has been time-reversed for simplicity).

### 4.3 The BdG Hamiltonian

The BdG matrix in equation (4.8) can be written in terms of Nambu-space Pauli matrices  $\tau_i$  in addition to the spin-space Pauli matrices  $\sigma_i$  to give the BdG Hamiltonian

$$H_{BdG} = [\eta p^2 + \alpha(\vec{\sigma} \times \vec{p}) \cdot \hat{z} + V_z \sigma_z - \mu] \tau_z + \Delta_n \tau_+ + \Delta_n^* \tau_-. \quad (4.9)$$

where  $\tau_{\pm} = \frac{1}{2}(\tau_x \pm i\tau_y)$ . Similarly, following the notation of Sau et al. [75] for consistency we define the ladder operator  $\sigma_{\pm} = \sigma_x \pm i\sigma_y$  and p-wave terms  $p_{\pm} = p_x \pm ip_y$ . In polar coordinates,  $p_{\pm} = e^{\pm i\theta}(-i\partial_r \pm \frac{1}{r}\partial_{\theta})$ , the single particle Hamiltonian is given by

$$H_0 = -\eta(\partial_r^2 + \frac{1}{r}\partial_r + \frac{1}{r^2}\partial_{\theta}^2) + \frac{i\alpha}{2}(\sigma_+ p_- - \sigma_- p_+) + V_z \sigma_z - \mu \quad (4.10)$$

and the pairing function is given by

$$\Delta_n(\mathbf{r}) = \sqrt{\Delta_0} \frac{p_+^2}{p_F^2} \sqrt{\Delta_0} = \frac{\Delta_0}{p_F^2} e^{in\theta/2} [e^{i\theta}(-i\partial_r + \frac{1}{r}\partial_{\theta})]^2 e^{in\theta/2} \quad (4.11)$$

$$= e^{i\theta(n+2)} \frac{\Delta_0}{p_F^2} [-i\partial_r + \frac{1}{r}\partial_{\theta} + i\frac{2+n}{2r}] [-i\partial_r + \frac{1}{r}\partial_{\theta} + i\frac{n}{2r}]. \quad (4.12)$$

The bound state wavefunction  $\Psi(r, \theta)$  around the vortex will be given by a solution to the time-independent BdG equation

$$H_{BdG}\Psi(r, \theta) = E\Psi(r, \theta). \quad (4.13)$$

with  $E = 0$ . This equation has an important “particle-hole symmetry” under the particle-hole operator  $P = K\sigma_y\tau_y$ ,

$$PHP^{-1} = -H \tag{4.14}$$

which implies eigenvalues of the BdG Hamiltonian come in pairs  $\pm E$ .

#### 4.4 Spin-Orbit-Pseudospin

A crucial question for the existence of a bound state around a vortex is whether the angular dependence of the gap  $\Delta$  can be eliminated by a mere gauge transformation of the components  $u$  and  $v$  of the form,

$$u \rightarrow ue^{i\theta n/2} \tag{4.15}$$

$$v \rightarrow ve^{-i\theta n/2}. \tag{4.16}$$

Since the pair  $u, v$  must be single-valued in  $\theta$  this is possible if  $n$  is even, but not if  $n$  is odd. As Gurarie and Radzihovsky argue, for an even vortex, the extra terms created in gauging away the  $\theta$  dependence of the Hamiltonian can be smoothly deformed away, so that the situation is topologically equivalent to no vortex.

The question of non-trivial vortex is related to another quantity in this problem, which is the combined spin-orbit-pseudospin symmetry of the BdG equation.

This symmetry is given by the pseudospin operator

$$J_z = L_z + \frac{1}{2}(\sigma_z - (n+2)\tau_z). \quad (4.17)$$

This pseudospin operator generalizes the angular momentum so that it commutes with the Hamiltonian,

$$[J_z, H_{BdG}] = 0. \quad (4.18)$$

The  $\sigma_z$  in (4.17) comes from the Rashba spin-orbit coupling and  $n+2$  is the vorticity of the vortex combined with the  $l = 2$  angular momentum of the chiral d-wave Cooper pairing.

Since  $J_z$  commutes with the Hamiltonian, a solution to the time-independent BdG equation will be an eigenstate of  $J_z$ . If we apply the particle-hole transformation to the  $J_z$  operator we obtain

$$PJ_zP^{-1} = KL_zK + \frac{1}{2}(\sigma_y\sigma_z\sigma_y - (n+2)\tau_y\tau_z\tau_y) = -L_z - \frac{1}{2}(\sigma_z - (n+2)\tau_z) = -J_z. \quad (4.19)$$

Consequently, under particle-hole symmetry  $E, J_z \rightarrow -E, -J_z$  and a non-degenerate eigenstate with  $E = 0$  must have  $J_z = 0$ . We will therefore consider solutions  $\Psi(r, \theta)$  such that

$$J_z\Psi(r, \theta) = 0 \quad (4.20)$$

and

$$L_z \Psi(r, \theta) = \frac{1}{2}[-\sigma_z + (n + 2)\tau_z]\Psi(r, \theta). \quad (4.21)$$

Since  $L_z$  generates translations in the  $\theta$  direction, we can use this operator to eliminate angular dependence.

For the non-degenerate zero-mode state, we use (4.21) to eliminate  $\theta$  dependence as follows:

$$\Psi(r, \theta) = \exp[-iL_z\theta]\Psi(r) = \exp[-i(-\sigma_z + (n + 2)\tau_z)\theta/2]. \quad (4.22)$$

In order for  $\Psi(r, \theta)$  to be single valued in (4.22),  $n \pm 1$  must be an even integer, implying that  $n$  must be odd for a bound state solution (even if  $m \neq 0$ ). Thus, the condition we get from  $J_z = 0$  agrees with our discussion of Gurarie and Razihovsky above.

On the other hand, if we had combined spin-orbit coupling with p-wave superconductivity  $l = 1$  or if we did not have spin-orbit coupling, the bound state would require an even vortex and not produce a Majorana bound state.

## 4.5 Radial BdG Equation

Now, given the assumption that  $n$  is odd, we eliminate  $\theta$  dependence from the BdG Hamiltonian

$$H'_{BdG} = \exp [i(-\sigma_z + (n + 2)\tau_z)\theta/2] H_{BdG} \exp [-i(-\sigma_z + (n + 2)\tau_z)\theta/2]. \quad (4.23)$$

to obtain a  $\theta$  independent BdG equation within the particular  $J_z = 0$  eigenspace,

$$H'_{BdG}\Psi(r) = 0. \quad (4.24)$$

Commuting the exponential operator through the Hamiltonian in (4.23) gives us the expression

$$\begin{aligned} H'_{BdG} = & -\eta \left[ \partial_r^2 + \frac{1}{r} \partial_r - \frac{(-\sigma_z + (n + 2)\tau_z)^2}{4r^2} \right] \tau_z + \alpha \left[ i\sigma_y \left( \partial_r + \frac{1}{2r} \right) + \sigma_x \frac{n + 2}{2r} \tau_z \right] \tau_z \\ & + V_z \sigma_z \tau_z - \mu \tau_z \\ & + \tau_x \frac{\Delta_0}{p_F^2} \left( \partial_r - \frac{(n + 2)(\tau_z + 1) - \sigma_z}{2r} \right) \left( -\partial_r + \frac{(n + 2)\tau_z - \sigma_z + n}{2r} \right). \quad (4.25) \end{aligned}$$

Only the superconducting gap term in  $H'_{BdG}$  exchanges the electron and hole Nambu subspaces with the matrix  $\tau_x$ . Since there are potentially two  $E = 0$  solutions (due to particle-hole symmetry), but since our radial BdG Hamiltonian is real, we can assume the possible solutions can combine to give a real solution. If this real solution is non-degenerate then it must be preserved under the particle-hole operator

up to a sign,

$$P\Psi(r) = \sigma_y\tau_y\Psi(r) = \lambda\Psi(r) \quad (4.26)$$

where  $\lambda = \pm 1$ . Because of this particle-hole relationship, when  $\tau_x$  acts on the non-degenerate zero-energy state  $\Psi(r)$  we obtain

$$\tau_x\Psi(r) = \lambda\tau_x\tau_y\sigma_y\Psi(r) = \lambda\tau_z i\sigma_y\Psi(r). \quad (4.27)$$

Using the property in (4.27) in (4.25) we obtain a matrix diagonal in the Nambu space:

$$\begin{aligned} H''_{BdG} = & -\eta \left[ \partial_r^2 + \frac{1}{r}\partial_r - \frac{(-\sigma_z + (n+2)\tau_z)^2}{4r^2} \right] \tau_z + \alpha \left[ i\sigma_y \left( \partial_r + \frac{1}{2r} \right) + \sigma_x \frac{n+2}{2r} \tau_z \right] \tau_z \\ & + V_z \sigma_z \tau_z - \mu\tau_z + \frac{\Delta_0\lambda}{p_F^2} \left\{ \left( \partial_r - \frac{n+2-\sigma_z}{2r} \right) \left( -\partial_r + \frac{n-\sigma_z}{2r} \right) - \frac{(n+2)^2}{4r^2} \right\} \tau_z i\sigma_y \\ & - \frac{\Delta_0\lambda}{p_F^2} \left( \frac{n+2}{r} \partial_r - \frac{n+2}{2r} \right) i\sigma_y. \end{aligned} \quad (4.28)$$

Now we have a BdG Hamiltonian in which the electron and hole subspaces are decoupled, and we can solve a 2 by 2 matrix differential equation instead of a 4 by 4 equation.

## 4.6 Solving the BdG Equation in the Electron Sector

Given the particle-hole symmetry of the BdG problem, we only have to solve the BdG equation in the electron or hole subspace, so we will assume  $\tau_z = +1$  to



obtain a two by two matrix differential equation. We will also assume  $n = -1$  for simplicity. After replacing  $\Delta_0\lambda/p_F^2 \rightarrow \Delta'$ , the two by two electron part of the BdG Hamiltonian is given by

$$\begin{aligned}
H_e &= -\eta \left[ \partial_r^2 + \frac{1}{r} \partial_r - \frac{(-\sigma_z + 1)^2}{4r^2} \right] + \alpha \left[ i\sigma_y \partial_r + \sigma_+ \frac{1}{2r} \right] + V_z \sigma_z - \mu \\
&\quad + \Delta' \left\{ \left( \partial_r - \frac{1 - \sigma_z}{2r} \right) \left( -\partial_r - \frac{1 + \sigma_z}{2r} \right) - \frac{1}{4r^2} - \left( \frac{1}{r} \partial_r - \frac{1}{2r^2} \right) \right\} \quad (4.29) \\
&= -\eta \left[ \partial_r^2 + \frac{1}{r} \partial_r - \frac{(-\sigma_z + 1)^2}{4r^2} \right] + \alpha \left[ i\sigma_y \partial_r + \sigma_+ \frac{1}{2r} \right] + V_z \sigma_z - \mu \\
&\quad + \Delta' \left\{ -i\sigma_y \left( \partial_r^2 + \frac{1}{r} \partial_r - \frac{1}{4r^2} \right) - \sigma_x \frac{1}{r} \partial_r + \sigma_+ \frac{1}{2r^2} \right\}. \quad (4.30)
\end{aligned}$$

In matrix form, the BdG equation for the electron part of the Majorana zero mode is given by

$$\begin{bmatrix}
-\eta \left[ \partial_r^2 + \frac{1}{r} \partial_r \right] - \mu + V_z & \alpha \left( \partial_r + \frac{1}{r} \right) - \Delta' \left( \partial_r^2 + \frac{2}{r} \partial_r - \frac{5}{4r^2} \right) \\
-\alpha \partial_r + \Delta' \left( \partial_r^2 - \frac{1}{4r^2} \right) & -\eta \left[ \partial_r^2 + \frac{1}{r} \partial_r - \frac{1}{r^2} \right] - \mu - V_z
\end{bmatrix} \Psi_e(r) = 0 \quad (4.31)$$

In the following two sections, we will solve this equation inside and outside of the vortex core and find conditions for the existence of a Majorana zero mode in the  $d + id$  superconductor.

## 4.7 Inside the Vortex Core ( $\Delta' = 0$ )

For a radius  $r < \xi$  smaller than the coherence length,  $\Delta' = 0$  and (4.31)

becomes

$$\begin{bmatrix} -\eta \left[ \partial_r^2 + \frac{1}{r} \partial_r \right] - \mu + V_z & \alpha \left( \partial_r + \frac{1}{r} \right) \\ -\alpha \partial_r & -\eta \left[ \partial_r^2 + \frac{1}{r} \partial_r - \frac{1}{r^2} \right] - \mu - V_z \end{bmatrix} \Psi_e(r) = 0. \quad (4.32)$$

This equation admits a solution in terms of Bessel functions  $\Psi_e(r) = \begin{bmatrix} u_\uparrow J_0(zr) & u_\downarrow J_1(zr) \end{bmatrix}$

since the Bessel functions satisfy

$$\left( \partial_r^2 + \frac{1}{r} \partial_r \right) J_0(zr) = z^2 J_0(zr) \quad (4.33)$$

$$\left( \partial_r^2 + \frac{1}{r} \partial_r - \frac{1}{r^2} \right) J_1(zr) = z^2 J_1(zr) \quad (4.34)$$

$$\left( \partial_r + \frac{1}{r} \right) J_1(zr) = z J_0(zr) \quad (4.35)$$

$$\partial_r J_0(zr) = z \left( \partial_{zr}^2 + \frac{1}{zr} \partial_{zr} - \frac{1}{(zr)^2} \right) J_1(zr) = -z J_1(zr). \quad (4.36)$$

Using the Bessel equation relations we find

$$\begin{bmatrix} -\eta \left[ \partial_r^2 + \frac{1}{r} \partial_r \right] - \mu + V_z & \alpha \left( \partial_r + \frac{1}{r} \right) \\ -\alpha \partial_r & -\eta \left[ \partial_r^2 + \frac{1}{r} \partial_r - \frac{1}{r^2} \right] - \mu - V_z \end{bmatrix} \begin{bmatrix} u_\uparrow J_0(zr) \\ u_\downarrow J_1(zr) \end{bmatrix} \quad (4.37)$$

$$= \begin{bmatrix} [(-\eta z^2 - \mu + V_z) u_\uparrow + \alpha z u_\downarrow] J_0(zr) \\ [\alpha z u_\uparrow + (-\eta z^2 - \mu - V_z) u_\downarrow] J_1(zr) \end{bmatrix}. \quad (4.38)$$

The RHS of (4.38) can be zero only if

$$\begin{bmatrix} -\eta z^2 - \mu + V_z & \alpha z \\ \alpha z & -\eta z^2 - \mu - V_z \end{bmatrix} \begin{bmatrix} u_\uparrow \\ u_\downarrow \end{bmatrix} = 0, \quad (4.39)$$

which gives us the characteristic equation

$$(\eta z^2 + \mu)^2 - V_z^2 - \alpha^2 z^2 = 0 \quad (4.40)$$

for potential solutions. Since this equation is quadratic in  $z^2$  it will in general have two solutions. In the next section we will discuss matching this solution for  $r < \xi$  to a series solution for  $r > \xi$ .

#### 4.8 Outside the Vortex Core ( $\Delta' \neq 0$ )

For  $r > \xi$ , where  $\Delta' \neq 0$ , we can use a series solution to (4.31),

$$\Psi_e(r > \xi) = \frac{e^{zr}}{r^{1/2}} \sum_{n=0}^{\infty} \begin{bmatrix} A_n \\ B_n \end{bmatrix} \frac{1}{r^n} \quad (4.41)$$

By applying  $H_e$  to (4.41) we obtain an equation

$$\sum_{n=0}^{\infty} \begin{bmatrix} M_{\uparrow\uparrow} & M_{\uparrow\downarrow} \\ M_{\downarrow\uparrow} & M_{\downarrow\downarrow} \end{bmatrix} \begin{bmatrix} A_n \\ B_n \end{bmatrix} = 0 \quad (4.42)$$

where

$$M_{\uparrow\uparrow} = -\eta \left[ \partial_r^2 + 2z\partial_r + z^2 + \frac{1}{4r^2} \right] - \mu + V_z \quad (4.43)$$

$$M_{\uparrow\downarrow} = \alpha(\partial_r + \frac{1}{2r} + z) - \Delta'(\partial_r^2 + \frac{1}{r}\partial_r - \frac{3}{2r^2} + \frac{z}{r} + 2z\partial_r + z^2) \quad (4.44)$$

$$M_{\downarrow\uparrow} = -\alpha(\partial_r - \frac{1}{2r} + z) + \Delta'(\partial_r^2 - \frac{1}{r}\partial_r + \frac{1}{2r^2} - \frac{z}{r} + 2z\partial_r + z^2) \quad (4.45)$$

$$M_{\downarrow\downarrow} = -\eta \left[ \partial_r^2 + 2z\partial_r + z^2 - \frac{3}{4r^2} \right] - \mu - V_z \quad (4.46)$$

which leads to the recursion relations

$$M_n^{(0)} \begin{bmatrix} A_n \\ B_n \end{bmatrix} + M_n^{(1)} \begin{bmatrix} A_{n-1} \\ B_{n-1} \end{bmatrix} + M_n^{(2)} \begin{bmatrix} A_{n-2} \\ B_{n-2} \end{bmatrix} = 0 \quad (4.47)$$

$$M_1^{(0)} \begin{bmatrix} A_1 \\ B_1 \end{bmatrix} + M_1^{(1)} \begin{bmatrix} A_0 \\ B_0 \end{bmatrix} = 0 \quad (4.48)$$

$$M^{(0)} \begin{bmatrix} A_0 \\ B_0 \end{bmatrix} = 0 \quad (4.49)$$

where

$$M_n^{(0)} = \begin{bmatrix} -\eta z^2 - \mu + V_z & \alpha z - \Delta' z^2 \\ -\alpha z + \Delta' z^2 & -\eta z^2 - \mu - V_z \end{bmatrix} \quad (4.50)$$

$$M_n^{(1)} = \begin{bmatrix} 2z\eta(n-1) & -\alpha(n - \frac{3}{2}) + \Delta' 2z(n - \frac{3}{2}) \\ \alpha(n - \frac{1}{2}) - \Delta' 2z(n - \frac{1}{2}) & 2z\eta(n-1) \end{bmatrix} \quad (4.51)$$

$$M_n^{(2)} = \begin{bmatrix} -\eta[(n-2)(n-1) - \frac{1}{4}] & -\Delta'[(n-2)(n-2) - \frac{3}{2}] \\ \Delta'[(n-2)n + \frac{1}{2}] & -\eta[(n-2)(n-1) - \frac{3}{4}] \end{bmatrix}. \quad (4.52)$$

The recursion relations can be solved if (4.49) is satisfied. Consequently, solutions can exist if  $M^{(0)}$  has a vanishing determinant giving us another characteristic equation for  $z$ ,

$$(\eta z^2 + \mu)^2 - V_z^2 + (\alpha z - \Delta' z^2)^2 = 0. \quad (4.53)$$

which agrees with (4.40) for  $\Delta' = 0$ . The characteristic equations (4.40) and (4.53) determine the number of solutions which must be matched at  $r = \xi$  in order for a solution to exist.

## 4.9 Matching solutions at $r = \xi$

In this section we find the condition for a single non-degenerate solution to exist by using the characteristic equations (4.40) and (4.53) to find the number of solutions and comparing with the number of constraints at the boundary  $r = \xi$ .

Because our BdG Hamiltonian has second-order differential operators, matching solutions at  $r = \xi$  requires us to satisfy four equations:

$$\Psi_e(r = \xi_-) = \Psi_e(r = \xi_+) \quad (4.54)$$

$$\partial_r \Psi_e(r = \xi_-) = \partial_r \Psi_e(r = \xi_+) \quad (4.55)$$

Combined with the normalization condition, this gives five constraints on the solution  $\Psi_e(r)$ . A solution can therefore exist if there are 5 total linearly independent solutions between the  $r < \xi$  and  $r > \xi$  cases.

In the case  $\eta = 0$  we can easily solve the characteristic equations (4.40) and (4.53) in the cases  $\Delta' = 0$  and  $\Delta' \neq 0$  to obtain

$$z_{r < \xi} = \pm \frac{\sqrt{V_z^2 - \mu^2}}{\alpha} \quad (4.56)$$

$$z_{r > \xi} = \frac{\alpha}{2\Delta'} \pm \sqrt{\left(\frac{\alpha}{2\Delta'}\right)^2 \pm \frac{\sqrt{V_z^2 - \mu^2}}{\Delta'}} \quad (4.57)$$

For the choices  $\lambda = -1$  and  $V_z^2 > \mu^2$  so that  $\Delta' < 0$  this gives us 2 total solutions for  $r < \xi$  and 3 normalizable solutions for  $r > \xi$ . Therefore, a non-degenerate bound state solution to (4.13) exists for  $\eta = 0$ . There is also a bound state solution for  $\eta \neq 0$ , but the solution is much more complicated in that case.

The condition  $|V_z| > \mu$ , a strong perpendicular magnetic field, is the same necessary as in the work of Sau et al. making the conditions for a Majorana in Bi/Ni similar to the conditions in a topological insulator / superconductor system.

## 4.10 Conclusions

In this chapter we investigated whether or not a Majorana bound state can exist on a vortex in a 2D  $d_{xy} + id_{x^2-y^2}$  superconductor with spin-orbit coupling and a perpendicular magnetic field. This study was motivated by the recent proposal of  $d_{xy} + id_{x^2-y^2}$  pairing in the 2D Ni/Bi bilayer with strong spin-orbit coupling [24]. It had already been predicted that normal superconductivity, spin-orbit coupling, and a perpendicular magnetic field enable Majorana bound states on odd vortices in 2D [75], but we extended this result to the  $d_{xy} + id_{x^2-y^2}$ .

We found that the existence of the bound state depends heavily on spin-orbit pseudo-spin, because this quantity determines whether the bound-state wavefunction is singlevalued around the vortex. With spin-orbit coupling and a Cooper pairing with even angular momentum ( $l = 2$ ), the bound state wavefunction is singlevalued around an odd vortex. Without spin-orbit coupling, the bound state wavefunction is singlevalued around an even vortex and can be gauged away [76]. Consequently, our result makes sense when compared with a previous study that considered  $d_{xy} + id_{x^2-y^2}$  without a Rashba spin-orbit coupling term and found no zero-mode [74].

We use particle-hole symmetry and spin-orbit pseudo-spin symmetry to obtain a radial differential equation acting only on an electron wavefunction. We solve the equation for  $\Delta_0 = 0$  in the vortex and  $\Delta_0 \neq 0$  outside the vortex and match solutions at the edge of the vortex to find the condition for exactly one real solution to exist. Namely, the perpendicular magnetic field must be sufficiently strong. This may

be more possible for the Ni/Bi bilayer than an s-wave superconductor, since it has intrinsic TRSB.



## Bibliography

- [1] H.-H. Kung, R. E. Baumbach, E. D. Bauer, V. K. Thorsmølle, W.-L. Zhang, K. Haule, J. A. Mydosh, and G. Blumberg. Chirality density wave of the “hidden order” phase in URu<sub>2</sub>Si<sub>2</sub>. *Science*, 347(6228):1339–1342, 2015.
- [2] H. K. Onnes. Further experiments with liquid helium. 13:1910–1911, 1911.
- [3] W. Meissner and R. Ochsenfeld. Ein neuer Effekt bei Eintritt der Supraleitfähigkeit. *Naturwissenschaften*, 21(44):787–788, 1933.
- [4] L. N. Cooper. Bound electron pairs in a degenerate fermi gas. *Phys. Rev.*, 104(4):1189, 1956.
- [5] J. Bardeen, L. N. Cooper, and J. R. Schrieffer. Theory of superconductivity. *Phys. Rev.*, 108(5):1175, 1957.
- [6] J. G. Bednorz and K. A. Müller. Possible high  $T_c$  superconductivity in the Ba-La-Cu-O system. *Zeitschrift für Physik B Condensed Matter*, 64(2):189–193, 1986.
- [7] D. D. Osheroff, R. C. Richardson, and D. M. Lee. Evidence for a new phase of solid he<sup>3</sup>. *Phys. Rev. Lett.*, 28(14):885, 1972.
- [8] F. Steglich, J. Aarts, C. D. Bredl, W. Lieke, D. Meschede, W. Franz, and H. Schäfer. Superconductivity in the presence of strong Pauli paramagnetism: CeCu<sub>2</sub>Si<sub>2</sub>. *Phys. Rev. Lett.*, 43:1892–1896, Dec 1979.
- [9] N. Shirakawa, K. Murata, Y. Nishihara, S. Nishizaki, Y. Maeno, T. Fujita, J. G. Bednorz, F. Lichtenberg, and N. Hamada. Novel Hall-coefficient behavior insuperconducting Sr<sub>2</sub>RuO<sub>4</sub>. *Journal of the Physical Society of Japan*, 64(4):1072–1075, 1995.
- [10] T. M. Rice and M. Sigrist. Sr<sub>2</sub>RuO<sub>4</sub>: an electronic analogue of <sup>3</sup>He? *Journal of Physics: Condensed Matter*, 7(47):L643, 1995.

- [11] G. M. Luke, Y. Fudamoto, K. M. Kojima, M. I. Larkin, J. Merrin, B. Nachumi, Y. J. Uemura, Y. Maeno, Z. Q. Mao, Y. Mori, et al. Time-reversal symmetry-breaking superconductivity in  $\text{Sr}_2\text{RuO}_4$ . *Nature*, 394(6693):558, 1998.
- [12] P. W. Anderson. Theory of dirty superconductors. *Journal of Physics and Chemistry of Solids*, 11(1-2):26–30, 1959.
- [13] A. P. Mackenzie, R. K. W. Haselwimmer, A. W. Tyler, G. G. Lonzarich, Y. Mori, S. Nishizaki, and Y. Maeno. Extremely strong dependence of superconductivity on disorder in  $\text{Sr}_2\text{RuO}_4$ . *Phys. Rev. Lett.*, 80:161–164, Jan 1998.
- [14] P. Mazur and S. R. De Groot. On onsager’s relations in a magnetic field. *Physica*, 19(1-12):961–970, 1953.
- [15] E. Taylor and C. Kallin. Intrinsic Hall effect in a multiband chiral superconductor in the absence of an external magnetic field. *Phys. Rev. Lett.*, 108:157001, Apr 2012.
- [16] P. M. R. Brydon, D. S. L. Abergel, D. F. Agterberg, and V. M. Yakovenko. Loop currents from nonunitary chiral superconductivity on the honeycomb lattice. *arXiv:cond-mat.supr-con/1802.02280*, 2018.
- [17] J. Xia, P. T. Beyersdorf, M. M. Fejer, and A. Kapitulnik. Modified Sagnac interferometer for high-sensitivity magneto-optic measurements at cryogenic temperatures. *Applied physics letters*, 89(6):062508, 2006.
- [18] A. Fried, M. Fejer, and A. Kapitulnik. A scanning, all-fiber sagnac interferometer for high resolution magneto-optic measurements at 820 nm. *Review of Scientific Instruments*, 85(10):103707, 2014.
- [19] A. D. Fried. Relationship of time-reversal symmetry breaking to optical kerr rotation. *Phys. Rev. B*, 90(12):121112, 2014.
- [20] J. Xia, Y. Maeno, Peter T. Beyersdorf, M. M. Fejer, and A. Kapitulnik. High resolution polar Kerr effect measurements of  $\text{Sr}_2\text{RuO}_4$ : Evidence for broken time-reversal symmetry in the superconducting state. *Phys. Rev. Lett.*, 97:167002, Oct 2006.
- [21] E. R. Schemm, W. J. Gannon, C. M. Wishne, W. P. Halperin, and A. Kapitulnik. Observation of broken time-reversal symmetry in the heavy-fermion superconductor  $\text{UPt}_3$ . *Science*, 345(6193):190–193, 2014.
- [22] E. R. Schemm, R. E. Baumbach, P. H. Tobash, F. Ronning, E. D. Bauer, and A. Kapitulnik. Evidence for broken time-reversal symmetry in the superconducting phase of  $\text{URu}_2\text{Si}_2$ . *Phys. Rev. B*, 91:140506, Apr 2015.

- [23] E. M. Levenson-Falk, E. R. Schemm, Y. Aoki, M. B. Maple, and A. Kapitulnik. Polar Kerr effect from time-reversal symmetry breaking in the heavy-fermion superconductor  $\text{PrOs}_4\text{Sb}_{12}$ . *Phys. Rev. Lett.*, 120:187004, May 2018.
- [24] X. Gong, M. Kargarian, A. Stern, D. Yue, H. Zhou, X. Jin, V. M. Galitski, V. M. Yakovenko, and J. Xia. Time-reversal symmetry-breaking superconductivity in epitaxial bismuth/nickel bilayers. *Sci. Adv.*, 3(3):e1602579, 2017.
- [25] V. M. Yakovenko. Theory of the high-frequency chiral optical response of a  $p_x + ip_y$  superconductor. *Phys. Rev. Lett.*, 98(8):087003, 2007.
- [26] V. P. Mineev. Broken time-reversal symmetry in the superconducting state of  $\text{Sr}_2\text{RuO}_4$ . *Phys. Rev. B*, 76(21):212501, 2007.
- [27] C. Kallin and J. Berlinsky. Chiral superconductors. *Rep. Prog. Phys.*, 79(5):054502, 2016.
- [28] S. D. Sarma, M. Freedman, and C. Nayak. Majorana zero modes and topological quantum computation. *npj Quantum Information*, 1:15001, 2015.
- [29] N. P. Breznay, M. A. Steiner, S. A. Kivelson, and A. Kapitulnik. Self-duality and a Hall-insulator phase near the superconductor-to-insulator transition in indium-oxide films. *Proc. Nat. Acad. Sci.*, 113(2):280–285, 2016.
- [30] O. M. Corbino. Periodic resistance changes of fine metal threads which are brought together by alternating streams as well as deduction of their thermo characteristics at high temperatures. *Physikalische Zeitschrift*, 12:292–295, 1911.
- [31] E. Taylor and C. Kallin. Anomalous Hall conductivity of clean  $\text{Sr}_2\text{RuO}_4$  at finite temperatures. *J. Phys.: Conference Series*, 449(1):012036, 2013.
- [32] S. P. Cooke. Hall and Kerr effects at microwave frequencies. *Phys. Rev.*, 74:701–702, Sep 1948.
- [33] J. C. Amato. Dual-mode microwave cavity for measurements of harmonic power. *Rev. Sci. Instr.*, 49(1):122–123, 1978.
- [34] R. H. Caverly. Scattering matrix representation for the microwave Hall effect in the depolarization regime. *J. App. Phys.*, 58(8):3124–3128, 1985.
- [35] J. E. Coppock, J. R. Anderson, and W. B. Johnson. The microwave Hall effect measured using a waveguide tee. *J. App. Phys.*, 119(10):105102, 2016.
- [36] J. Pearl. Current distribution in superconducting films carrying quantized fluxoids. *App. Phys. Lett.*, 5(4):65–66, 1964.
- [37] M. Bologna. Exact approach to uniform time-varying magnetic field. *Mathematical Problems in Engineering*, 2018.

- [38] A. Furusaki, M. Matsumoto, and M. Sigrist. Spontaneous Hall effect in a chiral p-wave superconductor. *Phys. Rev. B*, 64:054514, Jul 2001.
- [39] J. E. Hirsch. Electrodynamics of superconductors. *Phys. Rev. B*, 69:214515, Jun 2004.
- [40] J. A. Mydosh and P. M. Oppeneer. *Colloquium* : Hidden order, superconductivity, and magnetism: The unsolved case of URu<sub>2</sub>Si<sub>2</sub>. *Rev. Mod. Phys.*, 83:1301–1322, Nov 2011.
- [41] T. T. M. Palstra, A. A. Menovsky, J. van den Berg, A. J. Dirkmaat, P. H. Kes, G. J. Nieuwenhuys, and J. A. Mydosh. Superconducting and magnetic transitions in the heavy-fermion system URu<sub>2</sub>Si<sub>2</sub>. *Phys. Rev. Lett.*, 55:2727–2730, Dec 1985.
- [42] E. R. Schemm, R. E. Baumbach, P. H. Tobash, F. Ronning, E. D. Bauer, and A. Kapitulnik. Evidence for broken time-reversal symmetry in the superconducting phase of URu<sub>2</sub>Si<sub>2</sub>. *Phys. Rev. B*, 91:140506, Apr 2015.
- [43] K. Haule and G. Kotliar. Arrested Kondo effect and hidden order in URu<sub>2</sub>Si<sub>2</sub>. *Nature Phys.*, 5(11):796–799, 2009.
- [44] K. Haule and G. Kotliar. Complex Landau-Ginzburg theory of the hidden order in URu<sub>2</sub>Si<sub>2</sub>. *Europhys. Lett.*, 89(5):57006, 2010.
- [45] P. Chandra, P. Coleman, J. A. Mydosh, and V. Tripathi. The case for phase separation in URu<sub>2</sub>Si<sub>2</sub>. *J. Phys.: Condens. Matter*, 15(28):S1965, 2003.
- [46] A Amato, M. J. Graf, A De Visser, H Amitsuka, D Andreica, and A Schenck. Weak-magnetism phenomena in heavy-fermion superconductors: Selected  $\mu$ SR studies. *J. Phys.: Cond. Matt.*, 16(40):S4403, 2004.
- [47] K. Matsuda, Y. Kohori, T. Kohara, K. Kuwahara, and H. Amitsuka. Spatially inhomogeneous development of antiferromagnetism in URu<sub>2</sub>Si<sub>2</sub>: Evidence from <sup>29</sup>Si NMR under pressure. *Phys. Rev. Lett.*, 87:087203, Aug 2001.
- [48] T. E. Mason, B. D. Gaulin, J. D. Garrett, Z. Tun, W. J. L. Buyers, and E. D. Isaacs. Neutron-scattering measurements of long-range antiferromagnetic order in URu<sub>2</sub>Si<sub>2</sub>. *Phys. Rev. Lett.*, 65(25):3189, 1990.
- [49] J.-G. Park, H.-C. Ri, K. Kuwahara, and H. Amitsuka. Thermal hysteresis in magnetization of single crystal URu<sub>2</sub>Si<sub>2</sub>. *J. Magn. Magn. Mater.*, 177:455 – 456, 1998. International Conference on Magnetism.
- [50] P. Coleman. Heavy fermions and the Kondo lattice: a 21st century perspective. *arXiv preprint arXiv:1509.05769*, 2015.
- [51] G. Bastien. *Interplay between magnetic quantum criticality, Fermi surface and unconventional superconductivity in UCoGe, URhGe and URu<sub>2</sub>Si<sub>2</sub>*. PhD thesis, Université Grenoble Alpes, 2017.

- [52] C. Bareille, F. L. Boariu, H. Schwab, P. Lejay, F. Reinert, and A. F. Santander-Syro. Momentum-resolved hidden-order gap reveals symmetry breaking and origin of entropy loss in URu<sub>2</sub>Si<sub>2</sub>. *Nature Commun.*, 5:4326, 2014.
- [53] Y. J. Jo, L. Balicas, C. Capan, K. Behnia, P. Lejay, J. Flouquet, J. A. Mydosh, and P. Schlottmann. Field-induced Fermi surface reconstruction and adiabatic continuity between antiferromagnetism and the hidden-order state in URu<sub>2</sub>Si<sub>2</sub>. *Phys. Rev. Lett.*, 98:166404, Apr 2007.
- [54] E. Hassinger, G. Knebel, T. D. Matsuda, D. Aoki, V. Taufour, and J. Flouquet. Similarity of the Fermi surface in the hidden order state and in the antiferromagnetic state of URu<sub>2</sub>Si<sub>2</sub>. *Phys. Rev. Lett.*, 105:216409, Nov 2010.
- [55] M. Yokoyama, H. Amitsuka, K. Tenya, K. Watanabe, S. Kawarazaki, H. Yoshizawa, and J. A. Mydosh. Competition between hidden order and antiferromagnetism in URu<sub>2</sub>Si<sub>2</sub> under uniaxial stress studied by neutron scattering. *Phys. Rev. B*, 72:214419, Dec 2005.
- [56] G. J. Nieuwenhuys. Crystalline electric field effects in UPt<sub>2</sub>Si<sub>2</sub> and URu<sub>2</sub>Si<sub>2</sub>. *Phys. Rev. B*, 35:5260–5263, Apr 1987.
- [57] P. Santini and G. Amoretti. Crystal field model of the magnetic properties of uru<sub>2</sub>si<sub>2</sub>. *Phys. Rev. Lett.*, 73:1027–1030, Aug 1994.
- [58] H.-H. Kung, S. Ran, N. Kanchanavatee, V. Krapivin, A. Lee, J. A. Mydosh, K. Haule, M. B. Maple, and G. Blumberg. Analogy between the “hidden order” and the orbital antiferromagnetism in URu<sub>2-x</sub>Fe<sub>x</sub>Si<sub>2</sub>. *Phys. Rev. Lett.*, 117:227601, Nov 2016.
- [59] M. Sundermann, M. W. Haverkort, S. Agrestini, A. Al-Zein, M. M. Sala, Y. Huang, M. Golden, A. de Visser, P. Thalmeier, L. H. Tjeng, et al. Direct bulk-sensitive probe of 5f symmetry in URu<sub>2</sub>Si<sub>2</sub>. *Proc. Nat. Acad. Sci. U.S.A.*, 113:13989–13994, 2016.
- [60] C. Broholm, J. K. Kjems, W. J. L. Buyers, P. Matthews, T. T. M. Palstra, A. A. Menovsky, and J. A. Mydosh. Magnetic excitations and ordering in the heavy-electron superconductor URu<sub>2</sub>Si<sub>2</sub>. *Phys. Rev. Lett.*, 58:1467–1470, Apr 1987.
- [61] N. P. Butch, J. R. Jeffries, S. Chi, J. B. Leão, J. W. Lynn, and M. B. Maple. Antiferromagnetic critical pressure in URu<sub>2</sub>Si<sub>2</sub> under hydrostatic conditions. *Phys. Rev. B*, 82:060408, Aug 2010.
- [62] Y. Dalichaouch, M. B. Maple, M. S. Torikachvili, and A. L. Giorgi. Ferromagnetic instability in the heavy-electron compound URu<sub>2</sub>Si<sub>2</sub> doped with Re or Tc. *Phys. Rev. B*, 39:2423–2431, Feb 1989.

- [63] Y. Dalichaouch, M. B. Maple, R. P. Guertin, M. V. Kuric, M. S. Torikachvili, and A. L. Giorgi. Ferromagnetism and heavy electron behavior in  $\text{URu}_{2-x}\text{M}_x\text{Si}_2$  ( $\text{M} = \text{Re}, \text{Tc}$  and  $\text{Mn}$ ). *Phys. B: Condens. Matter*, 163(1):113–116, 1990.
- [64] N. P. Butch and M. B. Maple. The suppression of hidden order and the onset of ferromagnetism in  $\text{URu}_2\text{Si}_2$  via Re substitution. *J. Phys.: Condens. Matter*, 22(16):164204, 2010.
- [65] N. P. Butch and M. B. Maple. Evolution of critical scaling behavior near a ferromagnetic quantum phase transition. *Phys. Rev. Lett.*, 103:076404, Aug 2009.
- [66] V. F. Correa, S. Francoual, M. Jaime, N. Harrison, T. P. Murphy, E. C. Palm, S. W. Tozer, A. H. Lacerda, P. A. Sharma, and J. A. Mydosh. High-magnetic-field lattice length changes in  $\text{URu}_2\text{Si}_2$ . *Phys. Rev. Lett.*, 109(24):246405, 2012.
- [67] K. H. Kim, N. Harrison, M. Jaime, G. S. Boebinger, and J. A. Mydosh. Magnetic-field-induced quantum critical point and competing order parameters in  $\text{URu}_2\text{Si}_2\text{S}$ . *Phys. Rev. Lett.*, 91:256401, Dec 2003.
- [68] M. Jaime, K. H. Kim, G. Jorge, S. McCall, and J. A. Mydosh. High magnetic field studies of the hidden order transition in  $\text{URu}_2\text{Si}_2$ . *Phys. Rev. Lett.*, 89:287201, Dec 2002.
- [69] A. Suslov, J. B. Ketterson, D. G. Hinks, D. F. Agterberg, and B. K. Sarma.  $H$ - $T$  phase diagram of  $\text{URu}_2\text{Si}_2$  in high magnetic fields. *Phys. Rev. B*, 68:020406, Jul 2003.
- [70] P. Chandra and P. Coleman. Hysteric order in the heavy-fermion compound  $\text{URu}_2\text{Si}_2$ . *Nature*, 493:621–626, January 2013.
- [71] P. Chandra, P. Coleman, and R. Flint. Hysteric order in  $\text{URu}_2\text{Si}_2$ : Hybridization with a twist. *Phys. Rev. B*, 91:205103, May 2015.
- [72] P. Das, R. E. Baumbach, K. Huang, M. B. Maple, Y. Zhao, J. S. Helton, J. W. Lynn, E. D. Bauer, and M. Janoschek. Absence of a static in-plane magnetic moment in the ‘hidden-order’ phase of  $\text{URu}_2\text{Si}_2$ . *New J. Phys.*, 15(5):053031, 2013.
- [73] K. A. Ross, L. Harriger, Z. Yamani, W. J. L. Buyers, J. D. Garrett, A. A. Menovsky, J. A. Mydosh, and C. L. Broholm. Strict limit on in-plane ordered magnetic dipole moment in  $\text{URu}_2\text{Si}_2$ . *Phys. Rev. B*, 89:155122, Apr 2014.
- [74] D. Lee and A. P. Schnyder. Structure of vortex-bound states in spin-singlet chiral superconductors. *Phys. Rev. B*, 93:064522, Feb 2016.
- [75] J. D. Sau, S. Tewari, R. M. Lutchyn, T. D. Stanescu, and S. D. Sarma. Non-abelian quantum order in spin-orbit-coupled semiconductors: Search for topological Majorana particles in solid-state systems. *Phys. Rev. B*, 82(21):214509, 2010.

- [76] V. Gurarie and L. Radzihovsky. Zero modes of two-dimensional chiral p-wave superconductors. *Phy. Rev. B*, 75(21):212509, 2007.